3-26-2015

Initial Implementation and Testing of a Tightly-Coupled IMU/Pseudolite System

James E. C. Kawecki

INITIAL IMPLEMENTATION AND TESTING OF A TIGHTLY-COUPLED IMU/PSEUDOLITE SYSTEM

THESIS

James E.C. Kawecki, Capt, USAF

AFIT-ENG-MS-15-M-025

DEPARTMENT OF THE AIR FORCE
AIR UNIVERSITY

AIR FORCE INSTITUTE OF TECHNOLOGY

Wright-Patterson Air Force Base, Ohio

AFIT-ENG-MS-15-M-025

INITIAL IMPLEMENTATION AND TESTING OF A TIGHTLY-COUPLED IMU/PSEUDOLITE SYSTEM

THESIS

Presented to the Faculty

Department of Electrical and Computer Engineering

Graduate School of Engineering and Management

Air Force Institute of Technology

Air University

Air Education and Training Command

in Partial Fulfillment of the Requirements for the

Degree of Master of Science in Electrical Engineering

James E.C. Kawecki, B.S.E.E.

Capt, USAF

March, 2015

AFIT-ENG-MS-15-M-025

INITIAL IMPLEMENTATION AND TESTING OF A TIGHTLY-COUPLED IMU/PSEUDOLITE SYSTEM

THESIS

James E.C. Kawecki, B.S.E.E.
Capt, USAF

Committee Membership:

J. F. Raquet, PhD
Chair

K. J. Kauffman, PhD
Member

Maj M. D. Seal, PhD
Member

AFIT-ENG-MS-15-M-025

Abstract

Currently, the 746th Test Squadrons (746th TS) Central Inertial and GPS Test Facility (CIGTF) operates one of the most accurate truth reference systems, called the CIGTF Reference System (CRS). CIGTF will be replacing the CRS with a new references system called UHARS (Ultra High Accuracy Reference System). UHARS will differ from CRS by adding the ability to use a non-GPS pseudolite system, as a new measurement source. This research effort describes the design of the extended Kalman filter which is developed in AFIT's SPIDER filter framework which implements a tightly-coupled pseudolite/INS filter.

Acknowledgements

First and foremost, I give thanks to the Lord and Savior Jesus Christ. He is, he was and he always will be. I would especially like to thank my wife and four children and the rest of my family. For without them, I would not be where I am today. I would also like to thank Dr. John Raquet and the entire ANT staff for their continual support, guidance, and direction. Lastly, Capt Jones, and Mr. Roadruck and the rest of the"ANT-lers", who were one of the greatest teams I have worked with.

James E.C. Kawecki

Table of Contents

Page

Page

List of Figures

INITIAL IMPLEMENTATION AND TESTING OF A
TIGHTLY-COUPLED IMU/PSEUDOLITE SYSTEM

I. Introduction

1.1 Motivation

The Global Positioning System (GPS) is widely accepted as a valuable tool for position, navigation, and timing. As the system continues to proliferate, the threats to the system continue to likewise grow. This creates a need to develop alternative navigation systems that can continue to operate in a GPS degraded or denied environments. This generates the requirement to develop a system that operates for test systems in GPS degraded environments. One such alternative to relying on GPS for a truth reference is the currently emerging Ultra High Accuracy Reference Systems (UHARS) [11]. The UHARS project is currently under development by the 746th Test Squadron Central Inertial and GPS Test Facility (CIGTF) and will be further discussed in Section 1.2. In the past, to test GPS under jammed conditions, only a single frequency was jammed in order to leave the remaining frequency to obtain a truth solution [28]. At other times, both frequencies would be jammed, and then the truth relies on a smoothed solution based on the inertial navigation system (INS). This system includes the use of ground-based transceivers, or pseudolites, to transmit the signals used to develop the navigation solution. By incorporating pseudolites, which operate on a different radio-frequency (RF) band, more realistic test scenarios can occur where all GPS RF bands are jammed or degraded.

1.2 Background

The 746th Test Squadron Central Inertial and GPS Test Facility (CIGTF) partnered with Locata and AFIT to develop an improved truth reference system. Shockley provides a linage of the navigation solution truth reference systems used by the 746th TS and Figure 1.1 illustrates the reference systems development [23]. Previously, CIGTF employed other reference systems to assess position, velocity, and time. The first system the CIGTF developed was the Completely Integrated Reference Instrumentation System (CIRIS) [18]. CIRIS was a Fortran based system, that depended on an INS with beacon measurements. The CIGTF replaced CIRIS in 1990 with the CIGTF High Accuracy Post-processing Reference System (CHAPS) [26]. This reference system was developed in 1990 and began to include GPS signals[23]. The CIGTF Reference System (CRS), replaced CHAPS in and is the current system [18]. CIGTF is near the completion of replacing the CIGTF Reference System (CRS) with the Ultra High Accuracy Reference System (UHARS) currently under development as the next generation truth reference system.

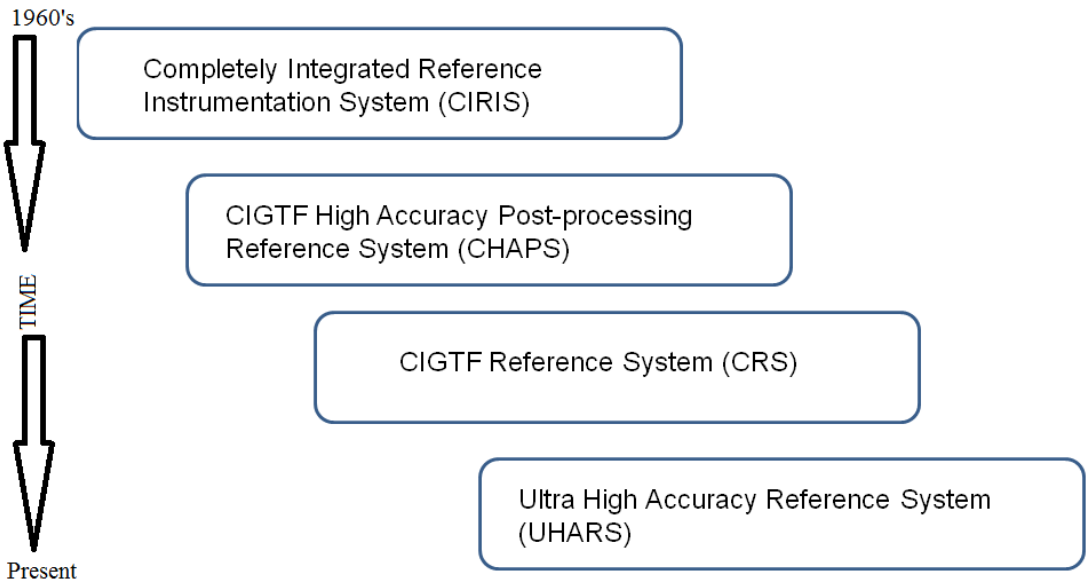

Figure 1.1. 746th Test Squadron Truth Reference Systems

1.3 Problem Definition

This research seeks to implement an algorithm to process pseudolite measurements tightly-coupled with an inertial measurement unit (IMU) or an inertial navigation system (INS) for obtaining a post-processed navigation solution. The pseudolite solution is expected to obtain a similar level of accuracy of GPS carrier-phase solutions[11]. The development of this new truth reference system must ultimately have the accuracy of at least the current systems accuracy under dynamic conditions. The UHARS set-up, further discussed in Chapter II and Chapter III, is capable for measuring positions for both ground and flight testing[23]. Data collected in early-November 2014 flight tests are used for this research. For the developed system, carrier-phase based navigation solutions were generated using the Sensor Processing and Inertial Dynamics Error Reduction (SPIDER) software written in $MATLAB^{®}$. This framework, discussed in Chapter III, allows for an expedited implementation of a Kalman filter.

1.4 Proposed Solution

In this research, measurements from the CRS and UHARS systems are processed and the results are analyzed. A tightly-coupled Locata Loclite/IMU navigation solution with cycle-slip detection and a state reset algorithm is developed and compared against the truth from the Novatel truth reference software Waypoint. The solution is analyzed against the truth to determine the accuracy of the developed algorithm. To implement the algorithm, the $MATLAB^{®}$-based SPIDER framework is employed. The results of the algorithm are further discussed in Chapter IV.

SPIDER.

The Sensor Processing and Inertial Dynamics Error Reduction (SPIDER) package for $MATLAB^{®}$, developed by AFIT, allows for quick implementation of new

navigation filter algorithms by having an established modular framework in place. Currently the SPIDER package allows the user to select sensors, and add scenario specific inputs as needed to a Kalman filter[25]. During this research effort a GPS differential carrier-phase solution and a Locata pseudolite carrier-phase model (including a pseudolite tropospheric delay model) are implemented in SPIDER and tested with inputs from test flight data.

1.5 Thesis Overview

Background information and a survey of literature is provided in Chapter II. The algorithms to model the pseudolite navigation solution and implemented tropospheric models are discuses in Chapter III. The processed results for the flight and ground tests are analyzed in Chapter IV. The results and discussion of the likely sources of error are analyzed as well. Chapter V suggests future work needed and summarizes relevance of this research.

II. Background

2.1 Introduction

This chapter presents the background information for the development of the navigation filter, failure detection/rejection algorithm, and the troposphere delay models for this research. In conducting the general outline of the research approach, previous works from AFIT were used [3][7][10].

2.2 Related Works

In 2004, Bouska developed simulations that studied the possibility that pseudolites can measure position accuracy to a 0.10 to 0.15 meter level [7]. Carrier-phase measurements were used in the simulation using floating-point ambiguities. Bouska's simulations focused on a pseudolite-only solution and were modeled using first-order Gauss-Markov functions to simulate both noise and uncertainty. Bouska stated in his research that centimeter-level accuracy is possible with a pseudolite only reference system. Further, a tropospheric scale factor error, which would appear to look like constant biases in the pseudolite measurements. This errors can be filtered by adding a state or states that would scale the tropospheric corrections by so linear factor [8]. His research has since provided a cornerstone for other research on pseudolite based navigation to include this document.

The optimal geometry of the Locata pseudolites has been evaluated by several researchers [12][13][32]. Crawford focused on using the geometric normalized accuracy of precision (GNAP) rather that the geometric dilution of precision (GDOP) as a metric[12]. Crawford showed through his research that an orbiting pseudolite, or an inverted pseudolite, holds promise to increase the level of precision. Having an orbiting pseudolite may not be always practical, so alternatively he showed that as

the elevation angle increased, the geometric errors decreased. Further, accuracy was also improved by the number of deployed pseudolites[12]. Dai further discussed the optimal geometry of the pseudolite positions, and also explored an inverted pseudolite configuration [13]. J.J. Wang discussed the near-far problem in consideration of the optimal design[32]. The near far problem is depicted in Figure 2.2.

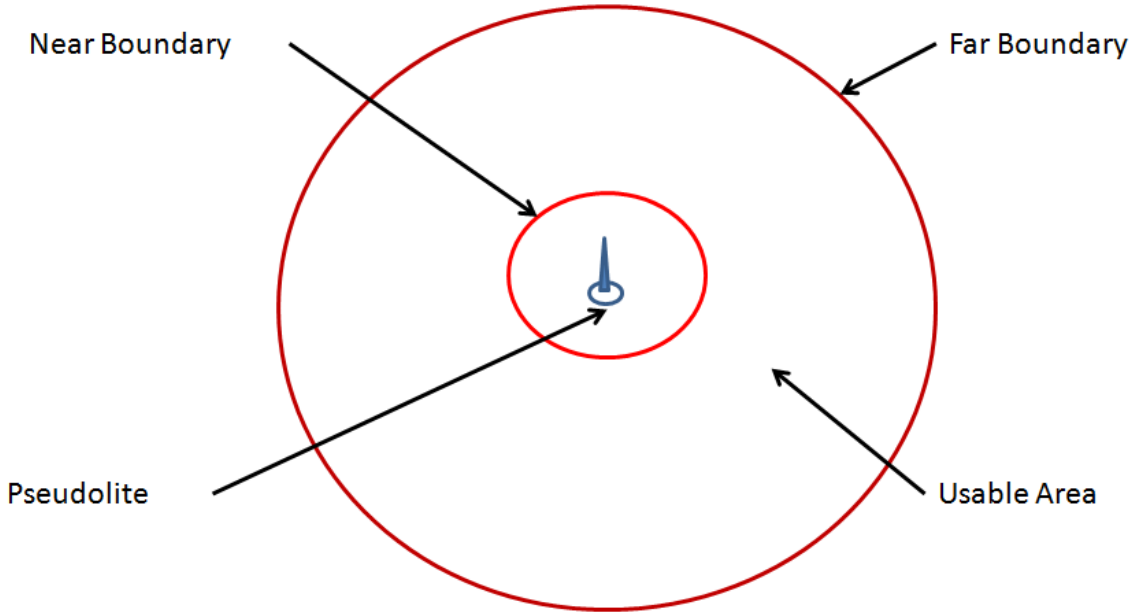

Figure 2.1. Near-Far Problem

The near-far problem, shown in Figure 2.1 illustrates the useable bounds of the pseudolites. For the purpose of this research effort, the aircraft's flight over the Loclite array is not affected by the near-far problem. In 2006 Amt using a Locata pseudolite only reference system demonstrated that ground and air vehicle positions could be accurately measured [3]. Amt used the carrier-phase measurements and pseudoranges to estimate the position solution. The pseudorange measurements applied a batch least squares algorithm, while the carrier-phase measurements were integrated using floating point ambiguity resolution in a Kalman filter. Further, the development of a height (altitude) determination for the pseudolite measurements contributed to the

overall progress of implementing the UHARS program. Shockley presented simulation and real data results for a Locata pseudolite positioning system that used single differenced carrier-phase measurements [3]. His research demonstrated that a pseudolite positioning system is capable of decimeter-level accuracy when the measurement errors are mitigated through modeling[4]. The tropospheric delay error, which Shockley chose to model by using a scale-factor in a manner similar to Bouska, allowed for results with improved accuracy[24]. In 2009, Ciampa furthered the existing research by proposing a failure detection algorithm for Locata pseudolites[10]. Ciampa compared failure detection residual monitoring algorithms based on thresholding and a moving window approach. After completion of his research, the recommendation was to use a combined approach of residual monitoring within the framework of a Kalman filter. Further discussion of residual monitoring is discussed in Section 2.8. Several researchers have performed a comparison of various pseudolite tropospheric delay models producing similar results[16] [31]. In Wang's research, the Radio Technical Commission for Aeronautics model (RTCA), modified RTCA, Bouska-Raquet, Saastamoinen, Niell mapping function and UNB3m models were compared by simulation [31]. The RTCA, Hopfield and Saastamoinen models were compared by So using flight test data with radiosonde meteorological data [16]. In both cases no single model's performance had the best overall results.

2.3 Navigation Reference Frames

A position and velocity trajectories are related in relative terms by using a reference frame. Below are descriptions of reference frame coordinate systems that are employed in this research. Figure 2.2 depicts the several reference frames defined for this research[27].

Earth Centered Earth Fixed.

The ECEF frame has the origin at the center of the Earth. The z-axis pints through the North Pole, the x-axis points to the intersection of the Equator and Prime-Meridian and the y-axis points orthogonal to both the x and z axes to complete the right-handed coordinate system[27]. The ECEF frame is used in this research when it is desirable to have all axis in units of meters. This is of particular interest when finding the distance between to objects. Figure 2.2 provides a visual of the ECEF reference frame along with the navigation reference frame [30].

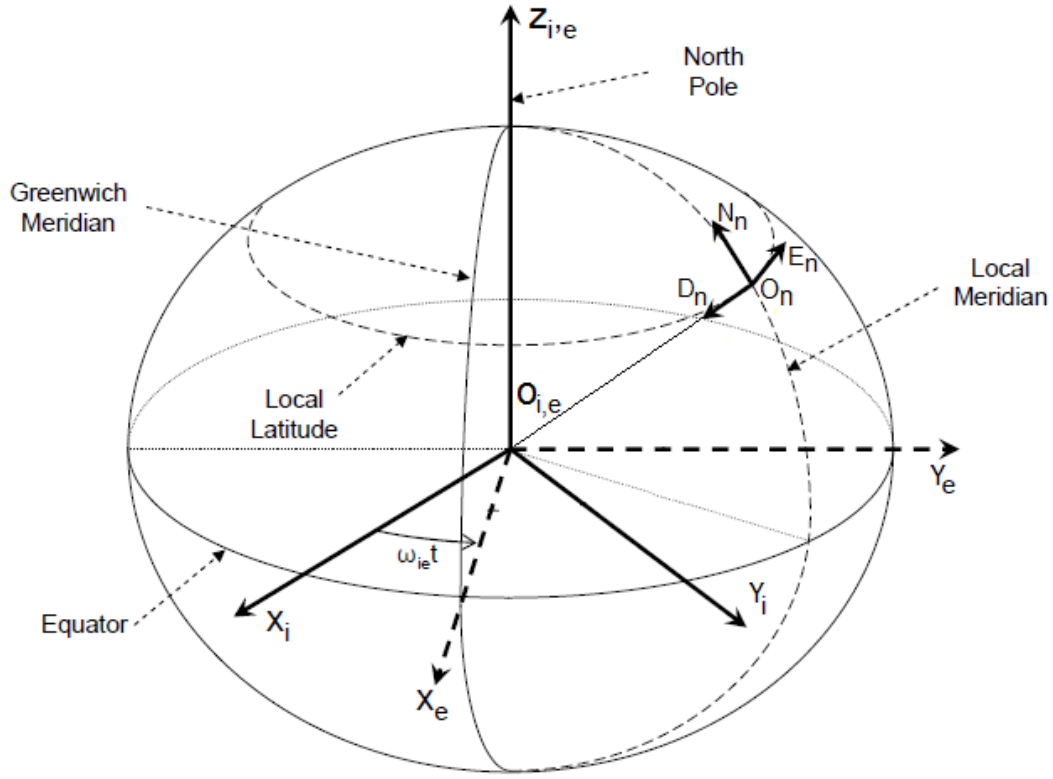

Figure 2.2. ECEF and Navigation Frames. Used with original author's permission[30].

Inertial Frame.

The o inertial frame like the ECEF has an origin at the center of the Earth. The z-axis of the inertial frame also points through the North Pole. The x-axis, points towards first star of Aries. The y-axis like in the ECEF points orthogonal to both the x and z axes completing the right-handed coordinate system [27].

Platform or Body Frame.

The platform or body frame reference frame uses the aircraft itself. The origin of the body frame located at the center of mass or some other fixed point of the aircraft. The x-axis points towards the nose of the aircraft, the y-axis points towards the right wing of the aircraft, and the z-axis point orthogonal to the x and y axis downwards[27]. The sensor frame is the frame in which the sensor measurements are directly measured. It can be related to the body frame through the use of lever arms (for translation) and also a relative orientation if needed[27].

Geodetic Coordinate system.

The geodetic coordinate system is a widely used reference frame. The axes this coordinate systems uses are fixed by the latitude and longitude lines of the Earth and an altitude off of the WGS-84 model[27].

2.4 Global Positioning System (GPS) Signals

The Global Positioning Systems is the current benchmark of high precision navigation reference systems. GPS satellites are identified by a unique pseudorandom noise (PRN) with a provided a navigation message. Within the navigation message, the satellites constellation's ephemeris is given so that the position of the satellite is known to some degree of error. The GPS satellites currently can transmit 3 fre-

quencies, however, two of the frequencies, often call the legacy frequencies, are used most widely for navigation solutions. These frequencies are the L1 (which operates at 1575.42 MHz) and L2 (which operates at 1227.6 MHz). The L1 frequency has both the course acquisition (C/A) and precise (P) codes, where the L2 frequency only carriers the P code. A GPS position solution most commonly achieves a position solution based on some combination of the following three measurements: pseudorange, carrier phase, and Doppler. The pseudorange and carrier-phase measurements are further discussed below.

Pseudorange Measurements.

The pseudorange measurements, or code measurements, are based on the difference between the time of the signal transmission and reception. The pseudorange measurements, although are widely available, have many errors associated with the measurements. Some of these errors include the troposphere delay error, ionosphere error, clock errors, measurement noise, multipath and variety of other errors factors [15][17]. Since several errors exist, the possibility exists that even a well modeled measurement will achieve a navigation solution for an air vehicle with approximately upwards of 10 meters of error[14]. The measurements for pseudorange is expressed as 2.1.

$$\rho = r + c(\delta t_m - \delta t_s) + T + m_\rho + v_\rho \tag{2.1}$$

where:

ρ = GPS pseudorange measurement ($meters$)

r = Range from the user's receiver to the transmitter ($meters$)

c = speed of light in a vacuum ($meters/second$)

δt_m = User clock error ($seconds$)

δt_p = Transmitter clock error ($seconds$)

T = pseudorange error due to Tropospheric delay

I = pseudorange error due to Ionospheric delay ($meters$)

m_ρ = pseudorange error due to multipath ($meters$)

v_ρ = pseudorange error due to receiver noise ($meters$)

Carrier-Phase Measurements.

The carrier-phase measurements are more accurate than pseudorange measurements since the noise and multipath are much smaller. Carrier-phase measurements are based on the number of cycles of the carrier frequency over the distance between the satellite and receiver. An integer ambiguity state, N, is created and becomes a source of error for the carrier-phase measurements until it is resolved. Once the integer ambiguity, is resolved, the integer ambiguity may suffer from cycle slips. When a cycle slip occurs the integer ambiguity typically is reset and must again reinitialize. The equation for carrier-phase measurements is expressed below in Equation 2.2[17].

$$\phi = \lambda^{-1}(r + c(\delta t_m - \delta t_p) + T + m_\phi + v_\phi) + N \tag{2.2}$$

where:

ϕ = carrier-phase measurement ($cycles$)

λ = carrier-phase wavelength ($cycles/second$)

m_ϕ = carrier-phase error due to multipath ($meters$)

v_ϕ = carrier-phase error due to receiver noise ($meters$)

N = carrier-phase integer ambiguity ($cycles$)

2.5 Pseudolites for Navigation

Interest in augmenting position, navigation and timing (PNT) infrastructures with pseudolites has been increasing [6]. When compared against GNSS, pseudolite are cost-efficient, relatively easy to field, and can provide the same level or better positioning accuracy [11]. Further, pseudolites can operate on separate radio frequency bands than GNSS and therefore can operate in GNSS jammed environments [5][6]. The pseudolites used in this research are Locata Loclites. The partnership between the 746th Test Squadron at Holloman AFB and the Locata Corporation has provided an opportunity to preform flight testing by the 746th TS culminating into the next generation flight reference system. Research from AFIT has made significant contributions to this framework since 2004 [21][3][10][24]. Figure 2.3 illustrates that the pseudolites operate on a 'master-slave' system. The master pseudolite time synchronizes all the slave pseudolite for precision timing.

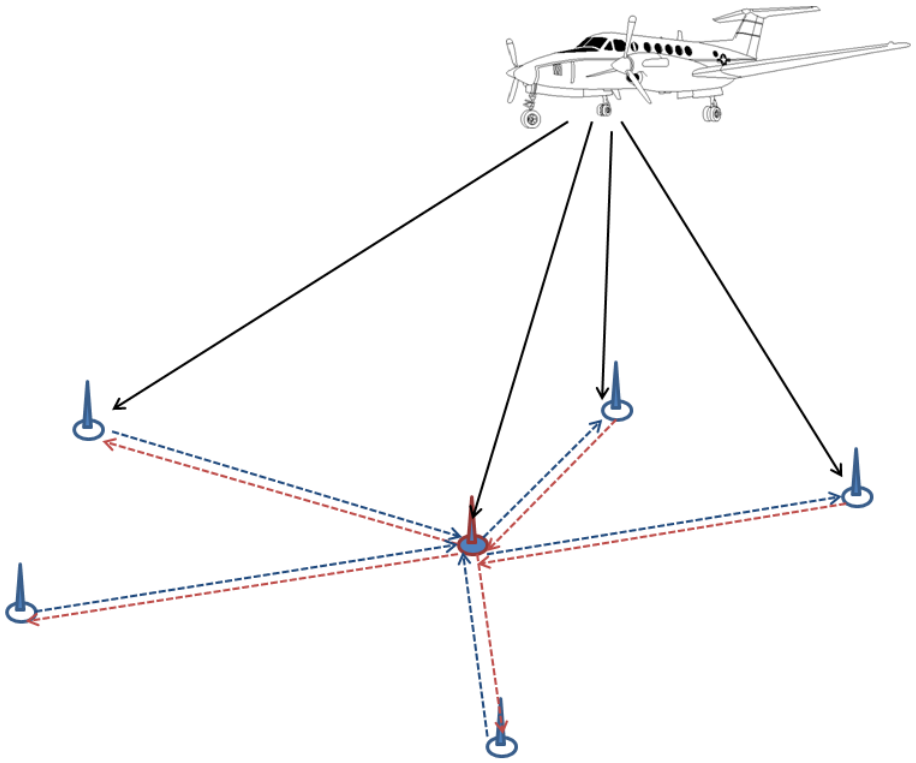

Figure 2.3. Locata Loclie Master-Slave Configuration

The pseudolites systems can generate the same observables as GPS; however, they are often ground-based systems. The pseudolites pseudorange and carrier-phase measurements at preformed just as the GPS measurement as explained above in Equation 2.1 and Equation 2.2. One significant change is that in the place of the GPS pseudorandom noise (PRN) as a method to identify the space vehicles, a naming convention was created for the pseudolites. The term, LRPN, is used for ease and commonality between GPS and the pseudolites.

2.6 Kalman Filter

The Kalman filter is a linear, optimal, recursive estimator that provides estimate over time. The estimates can either exist in continuous time or discrete time; however, for computational ease, the Kalman filter usually exist in a discrete fixed-time interval. The use of Kalman filtering is widely used for error-state navigation filters, particularly the extended Kalman filter. This section provides a brief description of the discrete Kalman filter algorithm[19].

The Discrete Kalman Filter Model.

For aviation, the Kalman filter often begins a known location of the aircraft. As the aircraft begins to move, the dynamics of the aircraft are propagated until a measurement from the INS/IMU or positioning system updates the location. The Kalman filter has two main components: the time update phase, or propagate, and the measurement correction phase, or update [9]. Additive white noise is introduced in both the propagation phase and during the measurement update. The propagation phase of the Kalman filter occurs at some defined interval in which the modeled systems dynamics are projected forward to the time of the next measurement. The state estimate at this time provides the *a priori* estimate for the next measurement incorporation. When the next measurement is available, the filter The Figure 2.4 depicts the cycle of the Kalman filter.

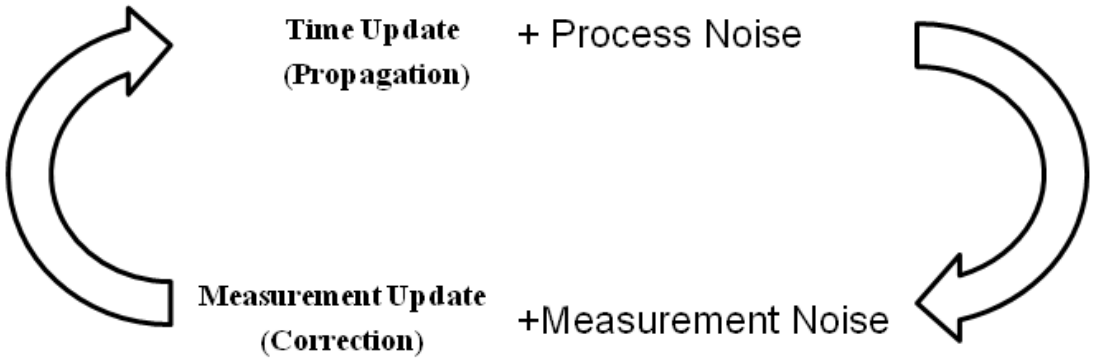

Figure 2.4. Kalamn Filter Cycle

By applying the linear differential equation characterized in linear time, is shown equation 2.3[19] . The input noise of the system's covariance is shown in equation 2.4 [19]

$$\dot{\mathbf{x}}(t) = \mathbf{F}\mathbf{x}(t) + \mathbf{G}\mathbf{w}(t) \tag{2.3}$$

$$\mathbf{Q}(t) = \mathrm{E}\left[\mathbf{w}(t)\mathbf{w}(t)^{\mathrm{T}}\right] \tag{2.4}$$

The system's dynamics that are modeled with states are represented by the $\mathbf{F}\mathbf{x}(t)$ in Equation 2.3. The system noise is represented by the $\mathbf{G}\mathbf{w}$(t) term, where $\mathbf{G}$ is the system noise mappi

$$\mathbf{P}_{\mathbf{xx}}(t) = \mathrm{E}\left[\mathbf{x}(t)\mathbf{x}(t)^{\mathrm{T}}\right] \tag{2.5}$$

$$\dot{\mathbf{P}}_{\mathbf{xx}}(t) = \mathbf{F}\mathbf{P}_{\mathbf{xx}}(t) + \mathbf{P}_{\mathbf{xx}}(t)\mathbf{F}^{\mathrm{T}} + \mathbf{G}\mathbf{Q}(t)\mathbf{G}^{\mathrm{T}} \tag{2.6}$$

Where $\mathbf{P}$ represents the state covariance matrix and the remaining terms have been previously defined. The next set of equations that the discrete KF usess are the equations to bring the filter into a discrete form. The variable k, represents the current discrete time. In Equation 2.7 , the state transition matrix is brought into a discrete form represented by the symbol $\mathbf{\Phi}$[19] . The noise also in brought into a

discrete form and is represented by the $\mathbf{Q}_{\mathrm{d}}$ represented by Equation 2.8.

$$\mathbf{\Phi} = e^{\mathbf{F}(\Delta t)_k} \tag{2.7}$$

$$\mathbf{Q}_{\mathrm{d}} = \mathrm{E}\left[\mathbf{w}_k \mathbf{w}_k^{\mathrm{T}}\right] \tag{2.8}$$

The next steps in the discrete KF is to apply the discrete state propagation and the discrete state covariance propagation shown in equations 2.9 and 2.10 .

$$\mathbf{x}_k = \mathbf{\Phi}\mathbf{x}_{k-1} + \mathbf{w}_k \tag{2.9}$$

$$\mathbf{P}_k = \mathbf{\Phi}\mathbf{P}_{k-1}\mathbf{\Phi}^{\mathrm{T}} + \mathbf{Q}_{\mathrm{d}} \tag{2.10}$$

The discrete state estimate, $\hat{\mathbf{x}}_k$ and the discrete covariance matrix, variance $\mathbf{P}_k$ is propagated forward in time. The previous estimated state mean and covariance matrix, represented by $\hat{\mathbf{x}}_{k-1}$ and $\mathbf{P}_{k-1}$ respectively, are applied to the Equations 2.11 and 2.12 . These equations then calculate the estimated state vector, and covariance represented by $\hat{\mathbf{x}}_k^-$ and $\mathbf{P}_k^-$.

$$\hat{\mathbf{x}}_k^- = \mathbf{\Phi}\hat{\mathbf{x}}_{k-1}^+ + \mathbf{w}_k \tag{2.11}$$

$$\mathbf{P}_k^- = \mathbf{\Phi}\mathbf{P}_{k-1}^+\mathbf{\Phi}^{\mathrm{T}} + \mathbf{Q}_{\mathrm{d}} \tag{2.12}$$

Once a measurement becomes available to the Kalman filter, the measurement updates can take place. The $\mathbf{z}_k$ term shows the filter's estimation of the desired state[19]. The $\mathbf{H}_k\mathbf{x}_k$ term represents where the state estimate is transformed into measurement space by the sensitivity matrix, $\mathbf{H}_k$, of a sensor, and the relationship to the states[19]. The measurement noise, $\mathbf{v}_k$, is typically defined by white Gaussian noise. Lastly the $\mathbf{R}_k$, or the measurement noise covariance matrix or measurement uncertainty covariance matrix, is defined by the type of sensor/measurement being used[9]. Equations

2.14 and 2.14 show how the linear measurement model f the KF and the noise covariance matrix are calculated.

$$\mathbf{z}_k = \mathbf{H}_k \mathbf{x}_k + \mathbf{v}_k \tag{2.13}$$

$$\mathbf{R}_k = \mathrm{E}\left[\mathbf{v}_k \mathbf{v}_k^{\mathrm{T}}\right] \tag{2.14}$$

The update phase of the KF is the last part of the KF algorithm. This phase, the measurement estimates, $\mathbf{z}_k$, are inputted into the algorithm to bring about a linear optimal estimate of the state estimates and state covariance estimates. The KF estimate is founded from a minimum mean square estimation error[9]. Equation 2.15 shows the Bayesian optimal estimate of

$$\hat{\mathbf{x}}_k^+ = \mathrm{E}(\mathbf{x}_k | \mathbf{z}_k) \tag{2.15}$$

The sensors measurements are feed into the Kalman filter at some time interval defined by each sensor. At this time interval a measure update occurs [9]. The Kalman gain, equation show in 2.16, *a posteriori* estimate covariance, equation shown in 2.17, and *a posteriori* state estimate are calculated, equation shown in 2.18.

$$K_k = \mathbf{P}_k^- \mathbf{H}_k^T (\mathbf{H}_k \mathbf{P}_k^- \mathbf{H}_k^T + \mathbf{R})^{-1} \tag{2.16}$$

$$\mathbf{P}_k^+ = (\mathbf{I} - K_k \mathbf{H}_k) \mathbf{P}_k^- \tag{2.17}$$

$$\hat{\mathbf{x}}_k^+ = \hat{\mathbf{x}_\mathbf{k}}^- K_k (\mathbf{z}_k - \mathbf{H}_k \hat{\mathbf{x}_\mathbf{k}}^-) \tag{2.18}$$

2.7 Extended Kalman Filters

The extended Kalman filter (EKF) is the extension of the Kalman filter that is able to estimate nonlinear state dynamics or measurements. The extended Kalman Filter

(EKF) is similar to the KF, in that the EKF also a recursive estimator that provide time based updates that is linearized around a estimate[9][20]. The extended Kalman filter unlike the Kalman filter, is sub-optimal, except when estimating linear problems, in which case is identical to the Kalman filter[20]. The EKF approaches nonlinearities by linearizing the state dynamics or measurement around a point. Each iteration the is linearized by a first-order Taylor series approximation of the nonlinearity. Further discussion of the EKF is found in [20].

Extended Kalman Filters Equations.

The propagation phase for the EKF consists of similar equations to that of the KF. The EKF propagate phase is much like that of of the KF; however, the state estimate, $\mathbf{f}(\hat{\mathbf{x}}_k)$, can be nonlinear. During the update phase updated by a non-linear function represented by $\mathbf{f}(\hat{\mathbf{x}}_k)$. The residual, sensitivity matrix, and Kalman gain differs from the KF shown in Equations 2.19, and 2.20.

$$\hat{\mathbf{x}}_k^+ = \hat{\mathbf{x}}_k^- + \mathbf{K}_k(\mathbf{z}_k - \mathbf{h}(\hat{\mathbf{x}}_k^-)) \tag{2.19}$$

$$\mathbf{P}_k^+ = (\mathbf{I} - \mathbf{K}_k\mathbf{H}_k)\mathbf{P}_k^- \tag{2.20}$$

The EKF measurement model, shown in Equation 2.21. is designed to handle nonlinearities. The state observabilities are mapped by the sensitivity matrix $\mathbf{Hx}_k$ within the KF algorithm and is replaced by passing the estimated states through a non-linear function $\mathbf{h}(\mathbf{x}_k)$[9][20]. The non-linear measurement function $\mathbf{h}(\hat{\mathbf{x}}_k)$ that passes through the EKF, is approximately linearized within the measurement matrix by the use of a first-order shown in Equation 2.22 Taylor series expansion.

$$\mathbf{z}_k = \mathbf{h}(\mathbf{x}_k) + \mathbf{v}_k \tag{2.21}$$

$$\mathbf{H}_k = \frac{\partial}{\partial \hat{\mathbf{x}}_k} \mathbf{h}(\hat{\mathbf{x}}_k) \tag{2.22}$$

2.8 Filtering Techniques

When running a EKF in MATLAB, processing time and numerical instability may become an issue. Techniques developed to counter some of these obstacles that arise is by using the upper diagonal matrix or the inverse covariance matrix[20].

Error States Model.

Rather that modeling the states of the actual measurement of the system's dynamics, it is advantageous to model the error states. Error state models are common techniques to model stochastic process, and are widely used for navigation. The error state are the simply put the difference between the 'truth' and the estimate. From error state models the truth, estimate, and error can be easily compared for analysis[9].

Residual Monitoring.

The integrity of a Kalman filter is entirely dependent on the ability to correctly model the system. One metric of a navigation filter's performance is the magnitude of the residuals. This thesis the residuals are monitored for both the carrier phase and pseudorange measurements and discussed in Chapter IV[20].

Upper Diagonal Factorization Matrix.

The U-D factorization implementation of the Kalman filter involves the use of an upper triangular matrix $\mathbf{U}$ and a diagonal matrix $\mathbf{D}$ defind in Equation 2.23[9].

$$\mathbf{P} = \mathbf{U}\mathbf{D}\mathbf{U}^T \tag{2.23}$$

Equation 2.23 is called the U-D factorization of $\mathbf{P}$. This allows the propagation and update of $\mathbf{U}$ and $\mathbf{D}$ instead of $\mathbf{P}$, decreasing the numerical issues in the implementation of the Kalman filter's algorithm. The variation of the matrix elements gets compressed so that the dynamic range is reduce. This results is higher efficiency to process the algorithm. The initial conditions start with $\hat{\mathbf{x}}(t_i^+)$ and $\mathbf{P}(t_i^+)$, and then finds $\mathbf{U}(t_i^+)$ and $\mathbf{D}(t_i^+)$ using U-D factorization. The propagation operation for the states follows the same as the KF.

Inverse Covariance Matrix.

The inverse covariance matrix is used when the values of the covariance become large. This technique is often used in optimal smoothing discussed below in Section 2.8.

Optimal Smoothers.

Optimal smoothing consists of three sub-types: fixed-point smoothing, fixed-interval smoothing, and fixed-lag smoothing[20]. The algorithm for fixed-point smoothing runs with selected points backwards in time. In fixed-interval smoothing, the algorithm run with a fixed time interval using *a posteriori* measurements. Fixed-lag smoothing, would be used if a near-real time filter is desired and the algorithm run on a delayed fixed time interval so that the real-time system can still estimate in real-time. In this research fixed-interval smoothing is the most appropriate smoothing algorithm for the post processed data analysis[20]. A fixed-interval Kalman smoother is divided into two parts, with the first part consisting of a standard KF running forward in time from the initial time t_0 to the final time t_f and the second part with a filter running backward in time from t_f to t_0. Upon completion of the forward and backward filter runs, the state estimates are optimally combined to create a

"smoother" estimate. For the forward filter, *a priori* information about $x(t_0)$ is used to initialize the KF, while for the backward filter, the "initial" condition is established with $x(t_f)$ as a random vector with no available *a priori* statistical information. A fixed-interval KF smoother requires one to estimate the states both forward and backward in time[20]. When implementing a backward KF, the covariance of the state at the final time (first time index for the backward method) is initialized to be infinite, meaning there is no information available about the states of the system. The derivation of the backward KF, using the inverse covariance form discussed in Section 2.8 and the optimal smoothing of the two KFs is found below. It begins by initializing the backward state estimate and the inverse covariance matrix to zero[20]. The fixed-interval Kalman smoother will produce the most optimal result possible[9]. This method is only valid in a post-test analysis since it requires all measurements from time initial to time final. This method requires more computational resources than the standard KF implementation, but in the post-test analysis environment this increase in computational overhead is not a significant concern. Kalman filters are recursive in nature, and run in forward time. The information that is taken into account currently in a Kalman filter is always from the previous time epoch.

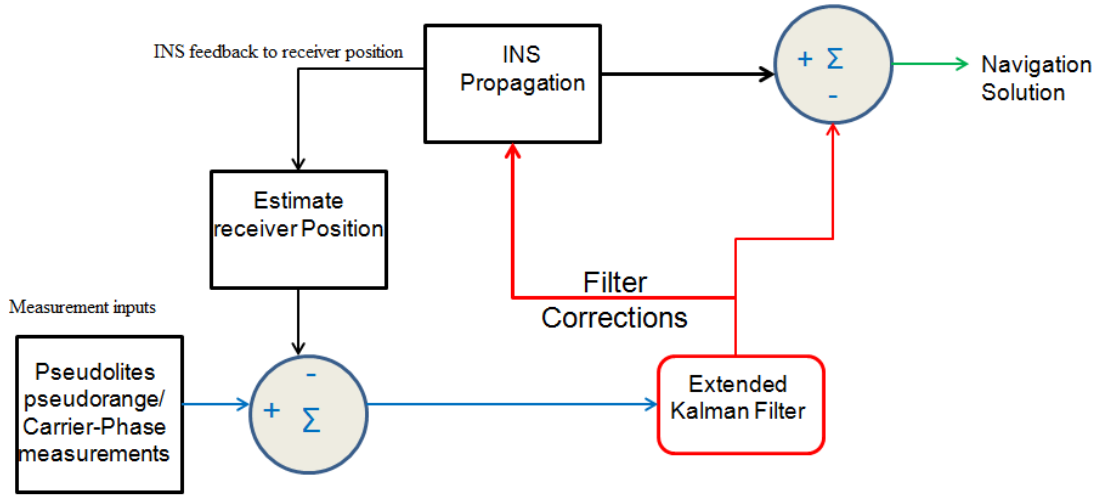

Figure 2.5. Reference Frames

2.9 Troposphere Delay Models

For navigation employing the use of pseudolites, the tropospheric delay becomes a major source of errors[11]. To achieve sub-decimeter level accuracy, the tropospheric model must be an appropriate estimation of the error induced upon the signal. The troposphere is a persistent source of error when propagating a radio frequency through this medium. Since the troposphere is a neutral, non-dispersive medium, the error caused by the delay of the signal can be modeled. To appropriately model the error, the troposphere must further be broken down into two components: the hydrostatic component, more commonly referred to the dry component; and the non-hydrostatic component, which is more commonly referred to as the wet component of the troposphere[31]. The dry component of the tropospheric error model consists of 80-90% of the error. The dry component is predictable based on the season (position of the Earth), altitude and general location of the receiver. Thus the dry component can be modeled in such a way to ensure that 99% of the error can be modeled for correctly. On the other hand, the wet component of the tropospheric error model only consists of 10-20% of the error, and generally is difficult to predict. It is from the difficultly of modeling the wet component of the troposphere that is the significant differentiator that separates the various troposphere delay models[16]. Several tropospheric delay models that are suitable for pseudolite positioning have been developed, however, the models fall into three categories. The first category is the integration method. An example of this method is the Hopfield model. The second category is this differencing method such as the modified RTCA model. The third category is the scaling method. In the scaling method, a scaling factor is added to the entire model in the state dynamics matrix. A comparison of these methods will be compared in this research and will be further discussed in Chapter III.

2.10 Summary

The information provided in this chapter provides the general overview of the signals and methods that will be used in development of the research. GPS and pseudolite signals, both having pseudorange and carrier measurements are inputs into the extended Kalman filter as will be presented in Chapter III.

III. Navigation Algorithm

3.1 Overview

This chapter lays out the development of the algorithms that implement the tightly-coupled pseudolite/INS integration. Descriptions of the state-models, measurement models, tropospheric model, and other necessary equations are contained in this chapter. The navigation filter is first examined.

Navigation Filter.

The navigation filter implemented in this research is derived from an extended Kalman filter, discussed in Chapter 2, implemented in the SPIDER framework, discussed in Chapter 1. The filter employs an error-state approach while tightly coupling the pseudolite measurements to the inertial measurements to reduce error. Although, the pseudolites measurement data is received at a 10 Hz rate, the measurements can be down sampled to any rate desired.

Inertial Model.

As discussed in Chapter II, state space modeling is a common method used for Kalman filtering. An error state model is developed to include all states of interest. By modeling the error states, rather than estimating the actual position, velocity, tilt angle, clock, and so on, this filter will rather output the errors of these states, this can then be applied to the inertial solution to obtain the final estimate.

State Dynamics Model.

The model used in this research is the Pinson-15. As stated in Chapter II [30], this model is an error states model of an IMU or INS. This research employes previ-

ously used model, the states consist of a three axis position, velocity, tilt, gyro bias, and acceleration bias[30]. These are computed in the navigation reference frame, as defined in Chapter II 2.3. The locations of the individual states are listed below to form the first 15-states of the state dynamics model, or the **F** matrix.

x_1 : Latitude (North) Position Error (rad)

x_2 : Longitude(East)Position Error (rad)

x_3 : Altitude (Down) Position Error (m)

x_4 : North Velocity Error (m/s)

x_5 : East Velocity Error (m/s)

x_6 : Down Velocity Error (m/s)

x_7 : North Tilt Angle Error (rad)

x_8 : East Tilt Angle Error (rad)

x_9 : Down Tilt Angle Error (rad)

x_{10} : X-axis Accel Bias/Error (m/s^2)

x_{11} : Y-axis Accel Bias/Error (m/s^2)

x_{12} : Z-axis Accel Bias/Error (m/s^2)

x_{13} : X-axis Gyro Bias/Error (rad/sec)

x_{14} : Y-axis Gyro Bias/Error (rad/sec)

x_{15} : Z-axis Gyro Bias/Error (rad/sec)

The state dynamic model, F_{INS} will form initially as a $15x15$ matrix as shown below in Equation 3.1. As other states are added, including clock error, and ambiguities,

the state dynamics model will grow while maintaining an $n - by - n$ matrix[30].

$$\mathbf{F_{INS}} = \begin{bmatrix} \mathbf{0}_{3x3} & \mathbf{I}_{3x3} & \mathbf{0}_{3x3} & \mathbf{0}_{3x3} & \mathbf{0}_{3x3} \\ \mathbf{C_e^n G C_n^e} & -2\mathbf{C n_e} \Omega_{ie}^e \mathbf{C_n^e} & f^n & 0_{3x3} & \mathbf{C_b^n} \\ \mathbf{0}_{3x3} & \mathbf{0}_{3x3} & -\mathbf{C_e^n} \omega_{ie}^e & -\mathbf{C^{n_b}} & \mathbf{0}_{3x3} \\ \mathbf{0}_{3x3} & \mathbf{0}_{3x3} & \mathbf{0}_{3x3} & \frac{1}{T_\omega}\mathbf{I}_{3x3} & \mathbf{0}_{3x3} \\ \mathbf{0}_{3x3} & \mathbf{0}_{3x3} & \mathbf{0}_{3x3} & \mathbf{0}_{3x3} & \frac{1}{T_a}\mathbf{I}_{3x3} \end{bmatrix} \tag{3.1}$$

where

$\mathbf{C}_n^e$: navigation to Earth frame rotation matrix

$\mathbf{C}_b^n$:body to navigation frame rotation matrix

$\mathbf{C}_e^n$: Earth to navigation frame rotation matrix

f^n: force in the navigation frame

$\mathbf{G}$: noise intensity matrix

Ω_e: Earth rate

T_a: time constant for accelerometer bias

T_ω: time constant for accelerometer bias

In addition to the states in the dynamics matrix is an accompanying system noise intensity matrix, or the $\mathbf{G}$ matrix. The noise intensity matrix describes the growth in the uncertainty over time and is dependent on the IMU/INS used for propagation. In this research an enhanced embedded global positioning system inertial navigation system(EEGI) is used. From the $\mathbf{G}$ matrix values, each states value will vary as the system propagates forward. Ideally, the $\mathbf{G}$ matrixs values correctly model the EEGIs actual noise characteristics. The Equations 3.2 and 3.3 removed the biases in the gyro and accelerometer noise, while Equation 3.4 models the drift in the accelerometer and

gyro[30].

$$\mathbf{f}_{ins}^{b} = f^{bias} + a_{bias} + w_{INS}^{f} \tag{3.2}$$

$$\omega_{ib_{ins}}^{b} = \omega_{bias} + \omega_{ib}^{b} + w_{INS}^{\omega} \tag{3.3}$$

$$\mathbf{a}_{bias} = \dot{a}_{bias} + w_{bias}^{a} \tag{3.4}$$

where

f_{ins}^{b}: forces on the force measurements in the INS

f^{bias}: bias in the forces

a_{bias}: accelleration bias

w_{INS}^{f}: white guassian noise acting upon the forces

$\omega_{ib_{ins}}^{b}$: gyro forces in the body frame

ω_{bias}: gyro bias

w_{INS}^{ω}: white guassian noise on the gyro measurments

w_{bias}^{a}: white guassian noiise of the acceleration bias

The resulting initial noise intensity matrix results in the follow shown in Equation 3.5. With the following DCMs defined in literature and identity matrices [27].

$$\mathbf{G}_{INS} = \begin{bmatrix} \mathbf{0}_{3x3} & \mathbf{0}_{3x3} & \mathbf{0}_{3x3} & \mathbf{0}_{3x3} \\ \mathbf{C}_{b}^{n} & \mathbf{0}_{3x3} & \mathbf{0}_{3x3} & \mathbf{0}_{3x3} \\ \mathbf{0}_{3x3} & -\mathbf{C}_{b}^{n} & \mathbf{0}_{3x3} & \mathbf{0}_{3x3} \\ \mathbf{0}_{3x3} & \mathbf{0}_{3x3} & \mathbf{I}_{3x3} & 0_{3x3} \\ \mathbf{0}_{3x3} & \mathbf{0}_{3x3} & \mathbf{0}_{3x3} & \mathbf{I}_{3x3} \end{bmatrix} \tag{3.5}$$

Clock Error.

Clock error states are important when using both GPS and pseudolite measurements in order to reduce error. Two-states are added to the **F** and **Q** matrixes for the clock errors, one representing the clock bias, while the other represents the derivative of the clock bias or the clock drift. These states will be used directly in the measurement models of the GPS or pseudolite models [15]. The clock errors are modeled in the filter by Equation 3.6[29].

$$\begin{bmatrix} \hat{x}_{clk_1} \\ \hat{x}_{clk_2} \end{bmatrix} = \begin{bmatrix} 0 & 1 \\ 0 & 0 \end{bmatrix} \begin{bmatrix} x_{clk_1} \\ x_{clk_2} \end{bmatrix} + \begin{bmatrix} w_{clk_1} \\ w_{clk_2} \end{bmatrix} \tag{3.6}$$

GPS and Pseudolites.

The GPS error-states added will depend on which measurement method is being used. For pseudoranges, the clock error state model suffices. Carrier phase measurements do require additional states to estimate the ambiguities. Each carrier-phase estimate requires an additional state to estimate the cycle ambiguities. This states also provides insight into cycle slip detection and reset for updating the measurements in the case that a cycle slip occurs[26][29].

Final State Dynamics And Noise Intensity.

Now that as the applicable states are created, these matrices are used to propagate the filter forward in time by using the equations laid out previously in Chapter II. The dynamics matrix varies with each epoch depending on the number of phase ambiguities tracked, but will consist of at least 17 rows and columns consisting of

Pinson 15 terms, and the clock terms[30].

$$\mathbf{F} = \begin{bmatrix} \mathbf{F}_{INS15} & 0_{15xn} & 0_{15xn} \\ 0_{2x15} & \mathbf{F}_{clk}\ 2x2 & 0_{2xn} \\ 0_{nx15} & 0_{2xn} & \mathbf{F}_N\ nxn \end{bmatrix} \tag{3.7}$$

The augmented state vector that is derived from the dynamics matrix consists the diagonal of that matrix. The noise matrix consists of an $n - by - m$ matrix, where n is equal to the number of states in the $\mathbf{F}$ matrix, and m is equal to the number of measurements included.

3.2 Measurement Model

The measurement model is derived using the measurements available to the filter at a moment in time. In this research, the pseudoranges and carrier-phase measurements are commonly used. The $\mathbf{h}$, and linearized $\mathbf{H}$, matrices contains all values derived from the measurements that will update the filter with the equations as previously introduced in Chapter 2.

Ultimately, the $\mathbf{H}$ matrix will consist of an $m - by - n$ matrix where n is the number of states and m is equal to the number of measurements. In this filter the measurement matrix[30]. The measurement uncertainty or measurement noise are modeled in the R matrix. These values, like the values of the $\mathbf{G}$ matrix provides the appropriate noise when correctly modeled. All the errors are applied and the corrected measurements are non-linear. Since these measurements are non-linear, for each epoch the measurement model is linearized using a first order Taylor series approximation [30]. The pseudoranges uses the estimates from the clock error states and the location of the pseudolites to provide measurement updates to the filters position estimate of the mobile receiver. The final equation to derive a measurement

from a pseudorange input is shown in Equation 3.8[30].

$$\hat{\rho}_n = \sqrt{\{(x_n - \hat{x_u})^2 + (y_n - \hat{y_u})^2 + (z - \hat{z_u})^2\}} + \widehat{c\delta t} \tag{3.8}$$

The pseudorange postion estimate, $\hat{\rho}$, is base on the x_n, y_n, and z_n transmitter locations differenced from the estimated mobile receiver location (x_u, y_u, and z_u). The $\widehat{c\delta t}$ term represents the filter's estimated clock error in meters. The carrier phase measurements will carry addition states to estimate the ambiguities, described by the variable N_n in units of cycles. Depending on the frequency of the systems used, the cycles are converted into meters, by dividing the number of cycles by the wavelength of the frequency [29].

$$\hat{\phi}_n = \frac{1}{\lambda_n}\sqrt{\{(x_n - \hat{x_u})^2 + (y_n - \hat{y_u})^2 + (z - \hat{z_u})^2\}} + \hat{N}_n + \widehat{c\delta t} \tag{3.9}$$

The carrier-phase position estimate, $\hat{\phi}_n$, differs from the pseudorange position estimate by including a term to convert to units of cycles by dividing by the wavelength of the carrier, λ_n, and adding in the ambiguity term, N_n. The resulting $\mathbf{h}$ vector will appear with a combination of the pseudorange measurements and carrier-phase measurements from Equations 3.10[29].

$$\mathbf{h}[\hat{x}(t^-)] = \begin{bmatrix} \sqrt{\{(x_n - \hat{x_u})^2 + (y_n - \hat{y_u})^2 + (z - \hat{z_u})^2\}} + \widehat{c\delta t} \\ \vdots \\ \frac{1}{\lambda_n}\sqrt{\{(x_n - \hat{x_u})^2 + (y_n - \hat{y_u})^2 + (z - \hat{z_u})^2\}} + \hat{N}_n + \widehat{c\delta t} \\ \vdots \end{bmatrix} \tag{3.10}$$

The $\mathbf{H}$ matrix will appear with a combination of the pseudorange measurements and carrier-phase measurements after taking the Jacobian derivatives from Equations

shown in Equation 3.11[29].

$$\mathbf{H}[\hat{x}(t)] = \begin{bmatrix} \frac{x_n^\rho - x_u}{r_n} & \frac{y_n^\rho - y_u}{r_n} & \frac{z_n^\rho - z_u}{r_n} & 0 & \cdots & -1 & 0 & \cdots & 0 \\ \vdots & \vdots & \vdots & \vdots & \ddots & \vdots & \vdots & \vdots & \vdots \\ \frac{x_n^\rho - x_u}{r_n} & \frac{y_n^\rho - y_u}{r_n} & \frac{z_n^\rho - z_u}{r_n} & 0 & \cdots & -1 & 0 & \cdots & 0 \\ \frac{x_n^\phi - x_u}{r_n} & \frac{y_n^\phi - y_u}{r_n} & \frac{z_n^\phi - z_u}{r_n} & 0 & \cdots & 0 & 1 & \cdots & 0 \\ \vdots & \vdots & \vdots & \vdots & \ddots & \vdots & \vdots & \ddots & \vdots \\ \frac{x_n^\phi - x_u}{r_n} & \frac{y_n^\phi - y_u}{r_n} & \frac{z_n^\phi - z_u}{r_n} & 0 & \cdots & 0 & \cdots & \cdots & 1 \end{bmatrix} \tag{3.11}$$

This matrix was then converted to the latitude, longitude, and altitude states using the approach given in [22]. Note that the 1's in the last columns of the **H** matrix correspond to the ambiguity states associated with each measurement.

3.3 Lever Arms

When the navigation solution is calculated, it is often generated at the location of the sensor. In this research, the navigation solutions are generated at the inertial unit. The pointing vector from a sensor to the inertial unit is required to shift the navigation solution to a common point. This is accomplish by using direction cosine matrices and pointing vectors[30]. Figure 3.1 depicts the lever arms from an IMU to an RF receiver.

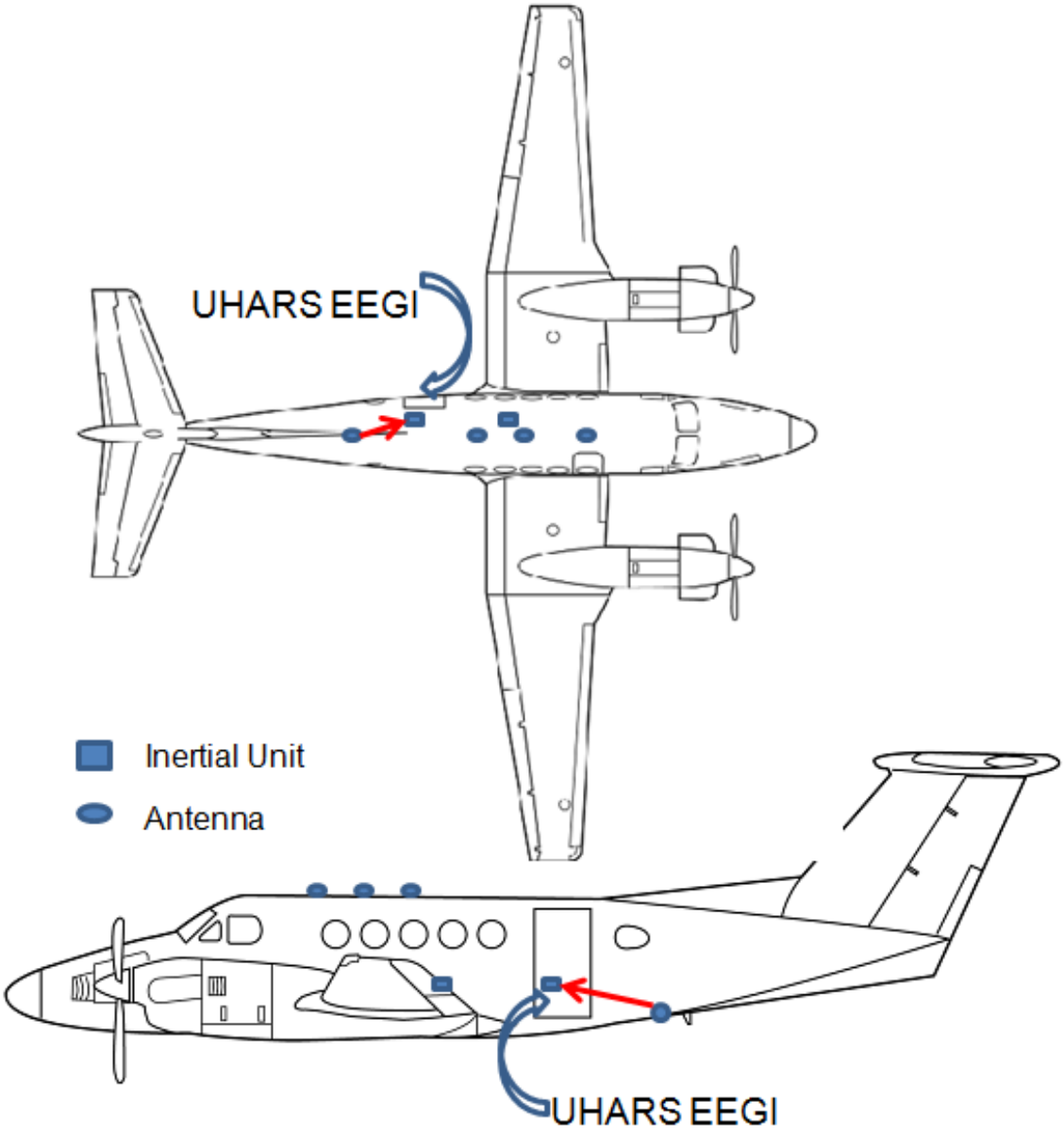

Figure 3.1. Example of Lever Arms from an Antennas to the Interial

3.4 SPIDER Filter Sequence

The EKF will run through the SPIDER framework in a multitude of steps [25]. First the specific parameters are inputted into the software. The parameters include, but are not limited to, the timeframe to run the filter, the sensors selected for the

measurement updates, noise values, lever arms, and tuning values. The states are then initialized following the model described in Section 3.2. The remaining filter states needed for the sensors are then initialized. These filter states include the clock terms, barometer, and carrier-phase ambiguities. The measurements then update the Kalman filer and and update the navigation solution. The output is then saved, and will continue for the remaining measurement epochs. If needed a final lever arm correction is applied to shift the solution to a desired location.

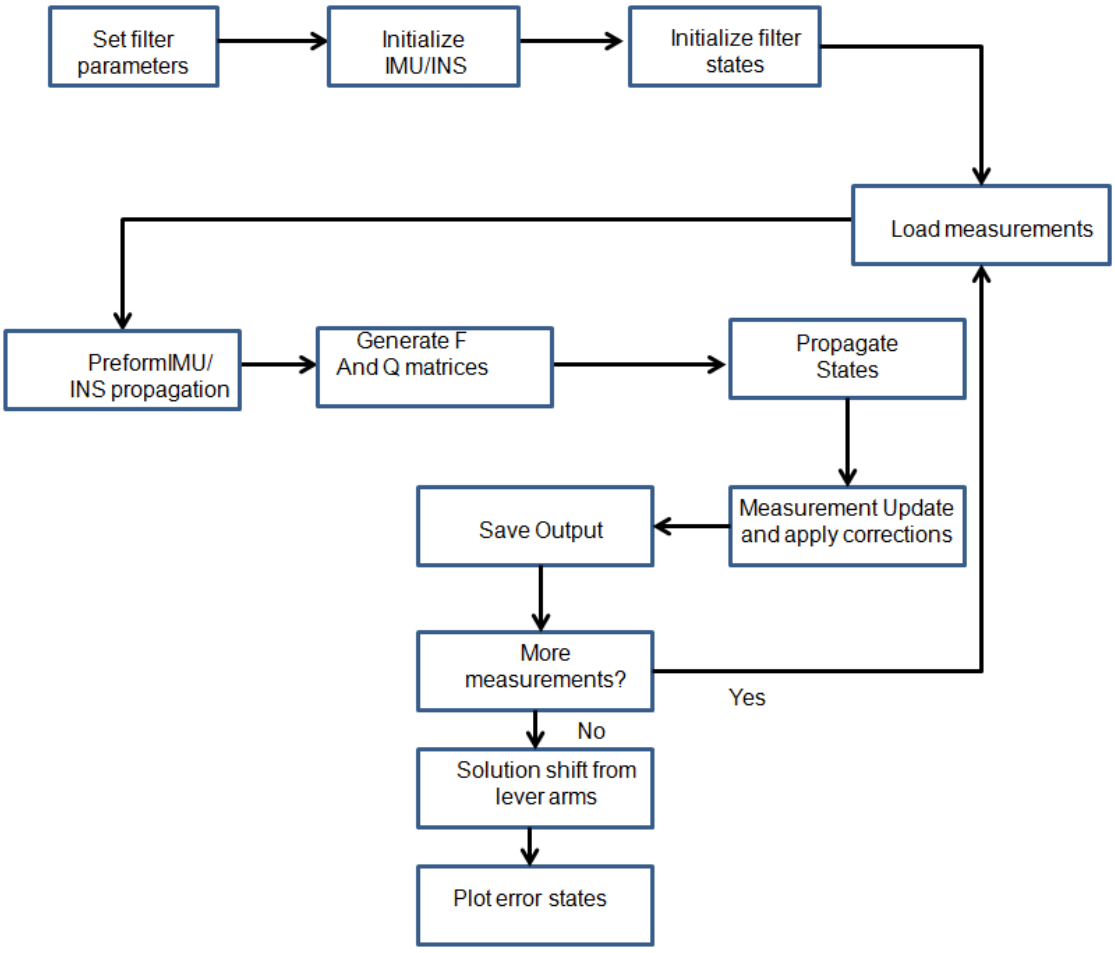

Figure 3.2. Spider Filter Sequence

3.5 Pseudolite Tropospheric Delay Models

Tropospheric delay as discussed in related works[11] [31], is a dominant error source for pseudolite based measurements. When calculating the tropospheric delay, the refractivity for the hydrostatic(dry) and non-hydrostatic(wet) components must first be calculated [31].

$$N_{dry} = 77.6 \cdot \frac{P}{T} \tag{3.12}$$

Where:

N_{Dry} is the dry refraction index of the medium

P is the pressure at the pseudolite measured in mmHG

T is the temperature in degrees Kelvin

$$N_{wet} = 22770 \cdot \frac{f}{T^2} \cdot 10^{\frac{7.4475(T-273}{T-38.3}} \tag{3.13}$$

Where:

N_{wet} is the wet refraction index

f is the relative humidity at the pseudolite

T is the temperature in degrees Kelvin

Although there exist several tropospheric models for tropospheric delay, three models were selected. The selected models were: a ray-tracing modified Hopfield model, the Bouska-Rauet model and an scaling model. These models at most only requires inputs of the altitude of the pseudolite, the model receiver, elevation angle, and the distance between the pseudolite and mobile receiver[16][8].

The modified Hopfield troposphere delay model is applied in a ray-tracing format is applied by calculating the altitude segment that the signal passes through. At each altitude segment, a delay term is estimated, and the sum of these terms are the final

estimate of the total tropospheric delay terms for that measurement. An illustration of this is seen in 3.3. The Hopfield model developed in 1969 has long been regarded as a well performing tropospheric delay model. The Hopfield model despite being one of the earliest differencing models is widely used still for GNSS. The equation for the Hopfield model is given in 3.14 and 3.15[31].

$$N_*^{trop}(h) = N_{*,0}^{trop}\left[\frac{h_* - h}{h*}\right]^4 \tag{3.14}$$

and

$$\Delta_*^{trop} = N_{*,0}^{trop}\int\left[\frac{h_* - h}{h_*}\right]10^{-6}ds \tag{3.15}$$

Where:

N_*^{trop}:refractivity

h:height

$N_{*,0}^{trop}$:refractivity at surface

h_*:scale height

Δ_*^{trop}:tropospheric delay

s: signal transmission path

Ray tracing allows the ability to segment the tropospheric delay area into smaller areas in order to obtain a better result[16]. This is done by diving the distance the height, h, of the mobile receiver to the pseudolite into n many segments. These segments will also correspond to a distance, r_n, between the transmitter and the mobile receiver. Then the r_n and h_n terms feed into the tropospheric delay models replacing the distance, R, and height, h, terms.

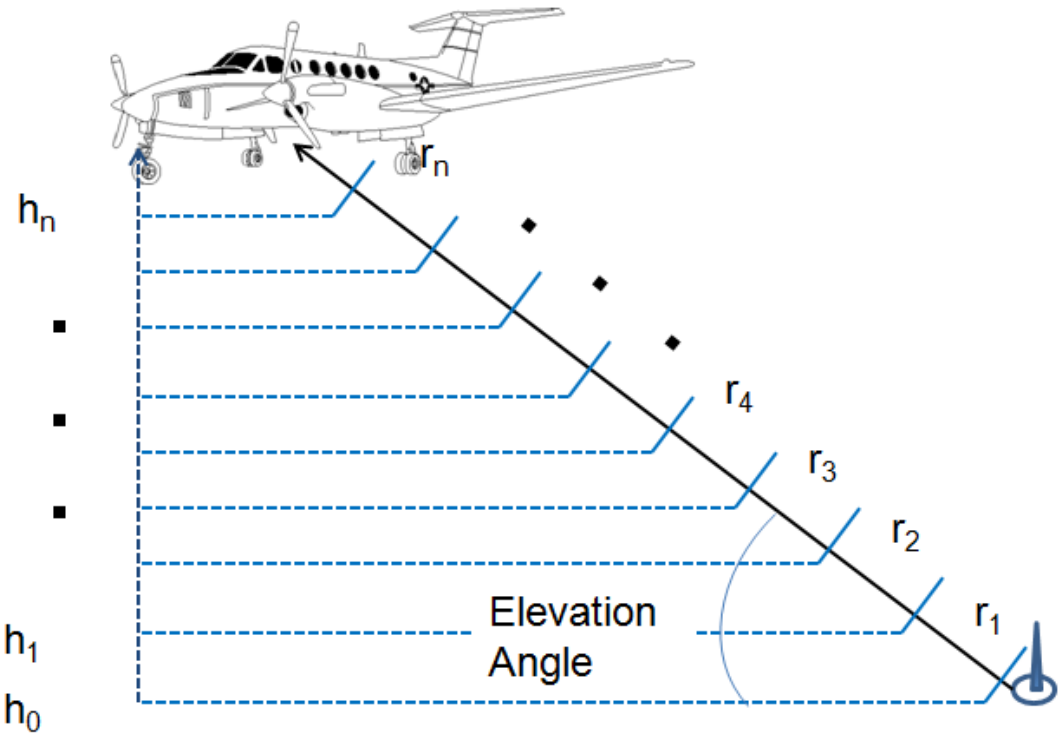

Figure 3.3. Ray tracing for Tropospheric Delay

The Bouska and Raquet model was developed based on the RTCA model from an internal memo for Van Dierendonck. This differencing method tropospheric delay model was developed in 2003 specifically for pseudolites. The equation is found in 3.16.

$$\Delta_{trop} = 2 \cdot 10^{-5} N R_u \frac{h_{*,0} - h_s}{\Delta h_u} \left[\left(1 - \frac{\Delta h_{APL}}{h_{*,0} - h_s} \right)^5 - \left(1 - \frac{\Delta h_{APL} - \Delta h_u}{h_{*,0} - h_s} \right)^5 \right] \quad (3.16)$$

Where:

Δ_{trop}:tropospheric delay

N:surface refractivity

R_u:range from pseudolite to reference receiver

$h_{*,0}$:scale height

h_s:height of the reference receiver

Ray tracing allows the ability to segment the tropospheric delay area into smaller areas in order to obtain a better result. This is done by diving the distance the height, H, of the mobile receiver to the pseudolite into n many segments. These segments will also correspond to a distance, r_n, between the transmitter and the mobile receiver. Then the r_n and h_n terms feed into the tropospheric delay models replacing the distance, R, and height, H, terms.

The index of refraction model is the scaling method of calculating the tropospheric delay[1]. The method apples a scale factor, and is given below in Equations 3.17, 3.18, and 3.19.

$$\Delta_{trop} = ND \cdot 10^{-6} \tag{3.17}$$

$$N_{wet} = 71.2962\frac{e_0}{T_0} + 375463\frac{e_0}{T_0^2} \tag{3.18}$$

$$N_{dry} = 77.689\frac{(P_0 - e_0)}{T_0} \tag{3.19}$$

3.6 Carrier Phase Cycle Slip Detection and Repair

A cycle slip detection and repair method is important for when correcting carrier phase measurements[3]. Multipath can cause a poor measurement resulting in a cycle slip. The other common cause of cycle slips in this data is that a phase loop lock is lost during the measurement epoch and thus causes the loss of that measurement, resulting in a cycle slip as defines in the developed algorithm. The cycle-slip detection algorithm is implemented using the current and previous epochs measured data [29]. By differencing the current and previous carrier phase measurement and then applying a mean Doppler correction term the slip threshold term is calculated. A carrier-phase threshold is set, and if the delta carrier-phase is found to be above the slip threshold, a cycle slip was declared, further referred to as a threshold slip. Further, cycle slips

are declare if two consecutive measurements were not present, further referred to as a time slip.

$$Slip = \phi_t - \phi_{t-1} + [(Dop_t + Dop_{t-1})/2] \cdot \delta t \tag{3.20}$$

Where

ϕ_t = carrier-phase measurement at current epoch($cycles$)

ϕ_{t-1} = carrier-phase measurement at previous epoch ($cycles/second$)

Dop_t = Doppler measurement at current epoch($meters$)

Dop_{t-1} = Doppler measurement at previous epoch($meters$)

δt = Time in seconds between epochs ($meters$)

In the case of threshold and time slips, the reinitialization process takes place. This process consists of reinitializing the carrier-phase ambiguity state. The reinitialize state in this algorithm is calculated by differencing the carrier phase measurement with the pseudorange measurement converted to cycles. Further, the off-diagonal covariance terms of the pseudolite are reset to zero[15]. The new ambiguity estimate is recalculated based of the difference between the carrier phase measurement and the estimated receiver position.

In the case of threshold and time slips, the repair process takes place. The repair process consists of re-initializing the carrier-phase ambiguity state. The reinitialize state in this algorithm is calculated by differencing the carrier phase measurement with the filter estimated position converted to cycles. Further, the covariance terms are reset to zero for that ambiguity and the variance term is also reinitialized.

3.7 Flight Tests

Data collection comprised of a series of flight tests over the pseudolite array. The flight test were accomplished over the test-range at Holloman AFB where the

pseudolites locations were established. The locations of the pseudolites based on a local-level frame as pictured below in Figure 3.4.

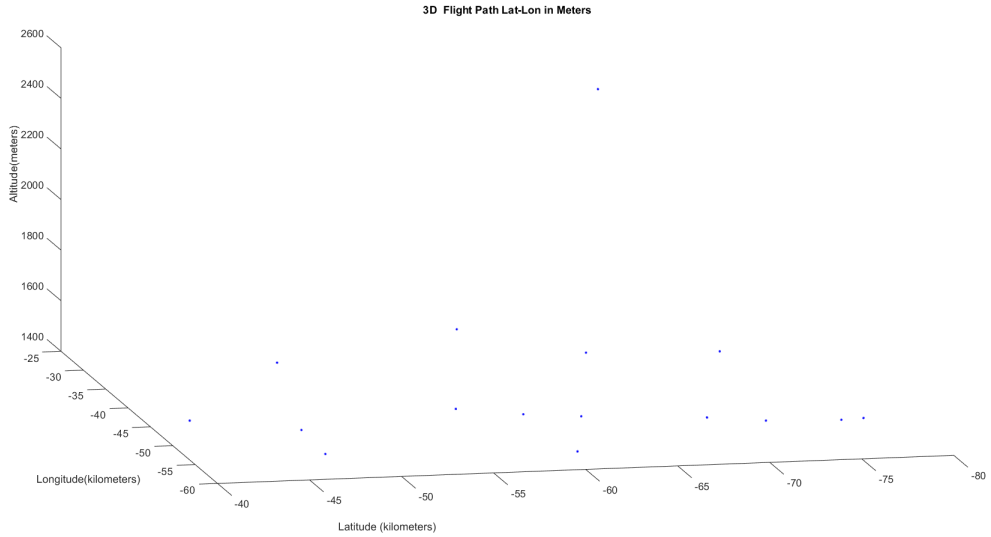

Figure 3.4. Loclite Array Over Flight Range

UHARS and CRS Pallets.

The CRS pallet is the current legacy pallet and consists of a Honeywell EEGI, Honeywell SNU and Trimble GPS receiver. The SNU is a navigation grade INS, and the EEGI achieves results higher than that of a tactical grade inertial. This configuration is proven to get decimeter level accuracy for flight testing. The UHARS pallet consists of a Honeywel EEGI, Trimble GPS receiver and the Locata Cooper antenna pseudolite receiver. A series of flight tests were accomplished in order to ensure multiple sets of data were collected.

3.8 Summary

This section summarized the algorithm and application of the measurement models to obtain the pseudolite navigation solution. The application of the developed

algorithms tropospheric delay models and cycle slip detection are a substantial important to this research.

IV. Navigation Filter Results and Analysis

4.1 Introduction

This chapter presents the results and analysis of the navigation filter employed for processing the data. The first section of this chatper discusses carrier-phased measurements from the pseudolites and the filters cycle slip detection and reset algorithm. The next section analyzes the effectiveness of various tropospheric delay models implemented during the course of developing the filter navigation solution. The following section discusses the navigation filter results from a variety of tests. Finally, a summary section closes this chapter.

4.2 Carrier-Phase Measurement Cycle Slip Detection and Repair

Carrier-phase measurements provide the greatest level of accuracy, but they are prone to cycle slips as previously discussed in Chapter 3. Cycle slips were categorized in one of two ways as previously discussed in Chapter 3: time base cycle slips and error magnitude threshold cycle slips. The cycle slips from exceeding the set threshold accounted for the majority of the slips. From Equation 3.20, the cycle-slip detection implementation worked without ever misidentifying a false-positive. Using slip thresholds, as defined in Equation 3.20 Chapter 3, of 1.5, and 3 wavelengths are later used for comparison in the developed tests. The wavelength of the frequency used is 0.1231 meters; therefore, the slip thresholds are equivalent to 18.47, and 36.94 centimeters. These thresholds were chosen to provide a constraint on the error to achieve a desired level of accuracy, while allowing for errors from other sources to include tropospheric error, clock errors, and unmodeled lever arm errors. Using too large of a slip threshold, as in the case of 5 cycles, or 61.57 centimeters, lead to a larger position error. Figures 4.1 and 4.2 show the position error of a 5-cycle and

1.5-cycle threshold respectivly, while keeping all other factors such as lever arms, and tropospheric delay model used constant.

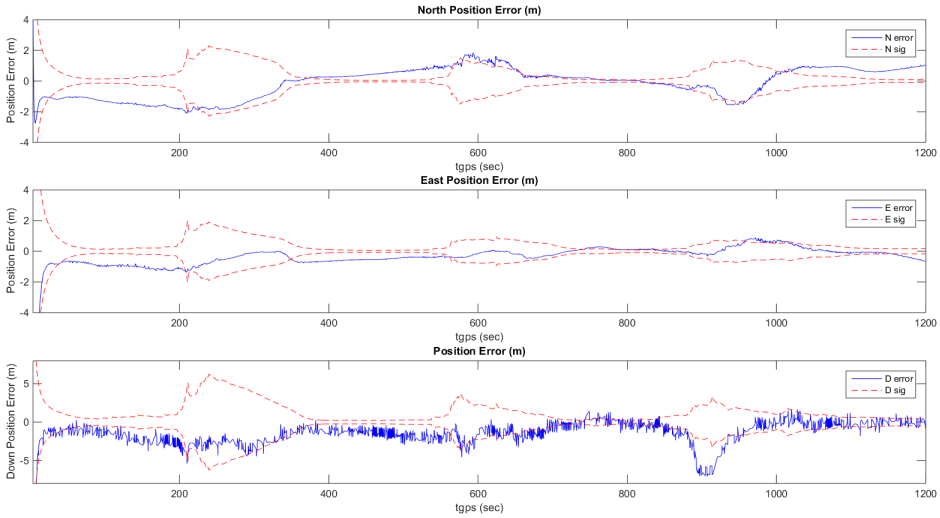

Figure 4.1. Position Error when a 5 Cycle-Slip Threshold is applied

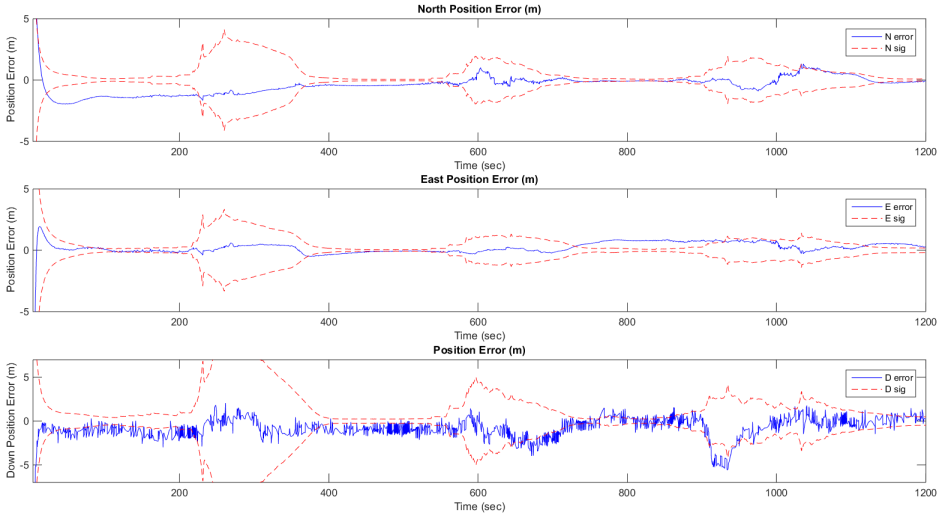

Figure 4.2. Position Error when a 1.5 Cycle-Slip Threshold is applied

Figure 4.12 shows an overall better position error when compared against Figure 4.1 through visual inspection. Further, for this test a 5-cycle threhold compared

against a 3-cycle threshold appeared very similar with outages occuring during the same times shown in Figures 4.3 and 4.4.

The change in the slip threshold, the number of slips varied from 2502 in the 1.5 cycle threshold case to 1550 in the 3 cycle threshold case, during the sample time period, however, the slips are generally located during the peroids where the aircraft is banking as demonstrated in Figures 4.3, and 4.4.

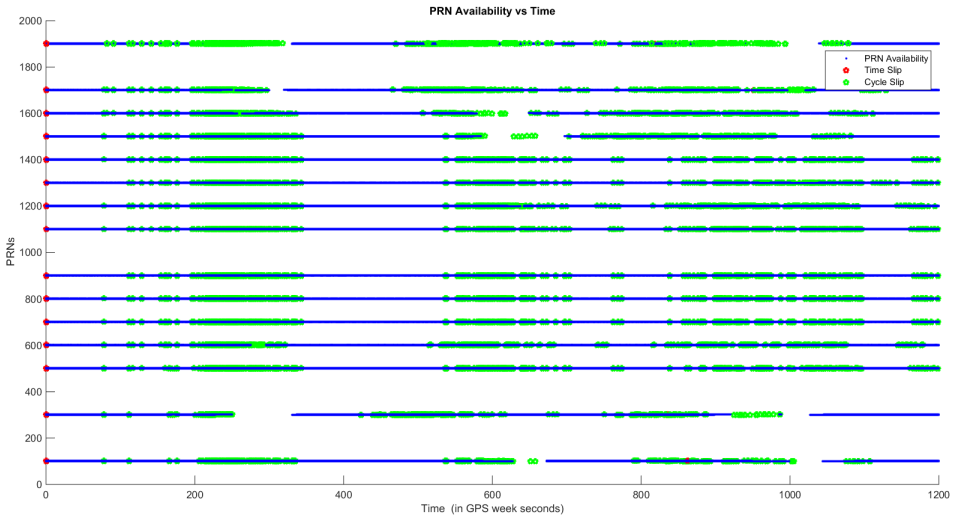

Figure 4.3. The LRPN Availability Showing Slip for a 1.5 Cycle-Slip Threshold

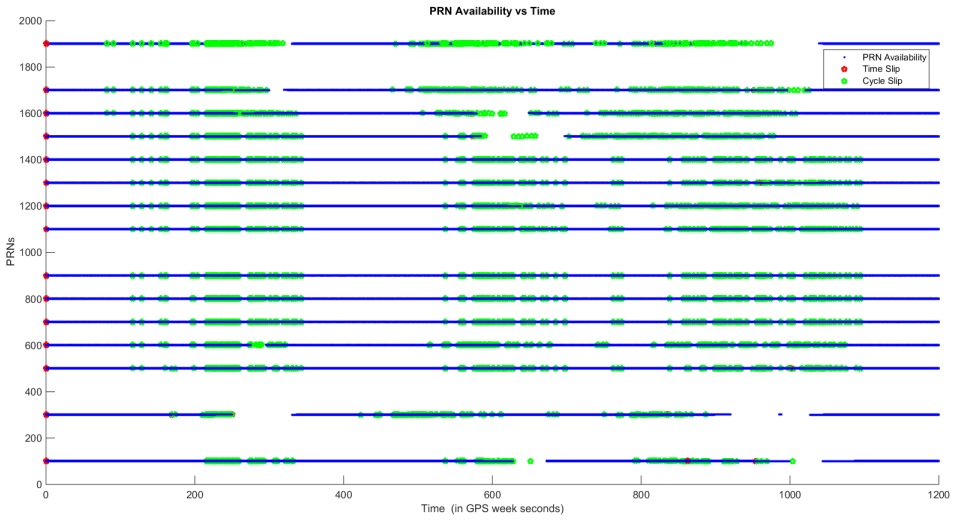

Figure 4.4. The LRPN Availability Showing Slip for a 5 Cycle-Slip Threshold

This implies that using larger slip thresholds led to higher initial position errors and does little to affect the impending cycle slips as the receiver loses lock on the pseudolite signal. Figures 4.3 and 4.4, with a slip threshold set to 5 cycles and 1.5 cycles respectively, demonstrates that position error significantly decreases with a higher cycle slip threshold, as does the uncertainty. This indicates that the filter is not detecting some cycle slips and thus allows the introduction of error into the position measurements.

The correlation between the aircrafts roll and cycle slips is most likely attributable to multipath caused from signals reflecting on the aircrafts fuselage or an error in the applied lever arms. Figure 4.5, plots the bank angle and the occurance of cycle slips.

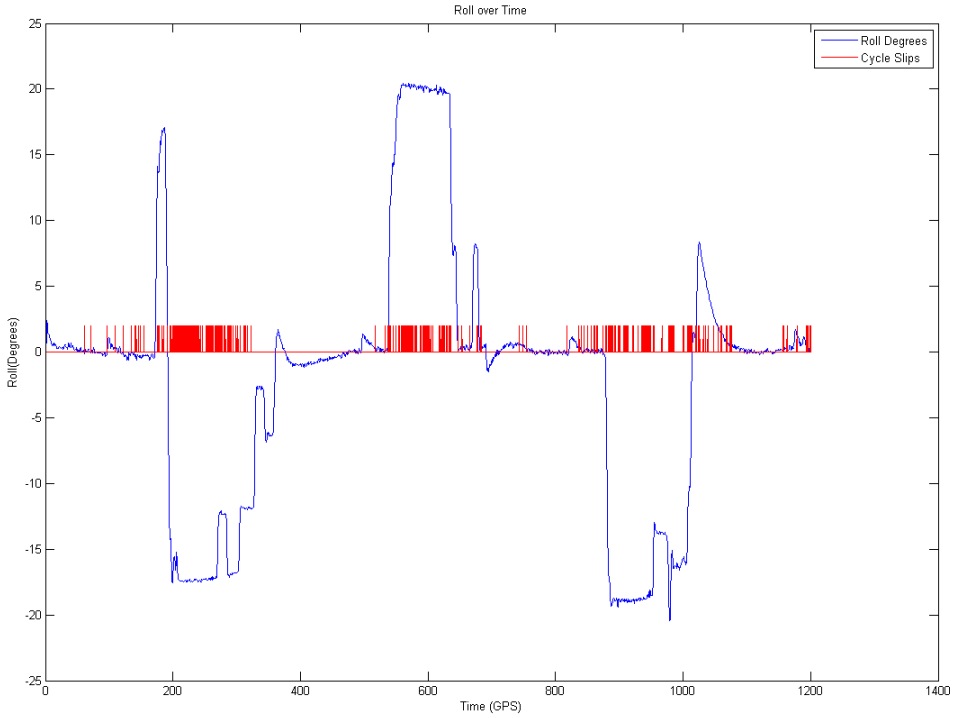

Figure 4.5. The Roll Angle of the Aircraft with Cycle Slips

Figure 4.5 shows that although cycle slips do not occur only during a banking maneuver; however, they are most prevalent during the peroids where the aircraft banks greater than 18 degrees. Further, since the banks are at the fringe of the range, the dilution of precision is higher as further discussed in Section 4.4.

The cycle slip repair process was implemented effectively. When examining the carrier phase ambiguities, the cycle repair process reset the state ambiguity to a new value, as well as resetting all cross correlation terms to zero. Figure 4.6 plots the change in the ambiguity estimates from the initial value after the cycle slip reset process against time. Cycle slips that exceeded a time threshold and cycle-slips that exceeded a cycle threshold are shown along with the ambiguity estimates change from the intial values.

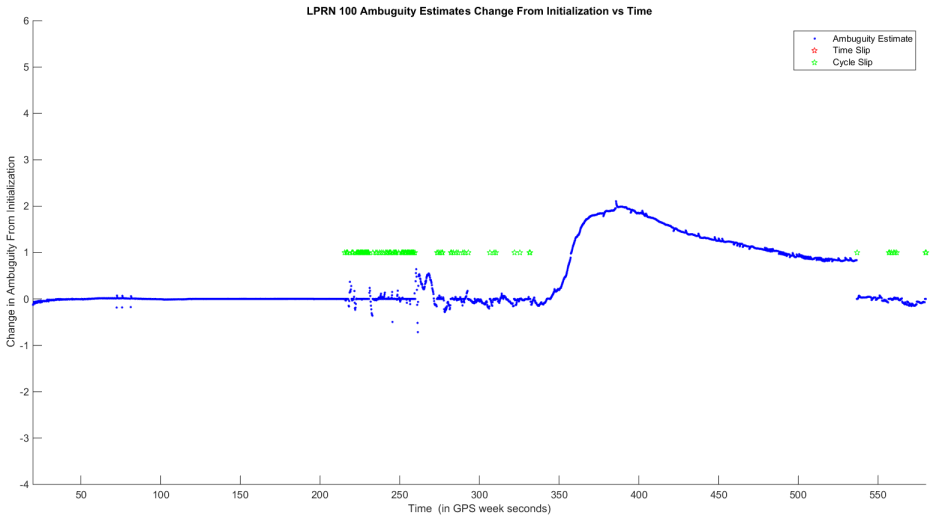

Figure 4.6. LPRN 100 Cycle Slips and Ambiguity Tracking

Figure 4.6 show the cycle slip repair process's effect on the ambiguities. The change from initial values of the ambiguities can change over several cycles; however, when considering the 10Hz data rate, each epoch change typically is only a tenth of a cycle.

4.3 Tropospheric Modeling

The tropospheric delay models used were a ray-traced approach based on the modified Hopfield model (RT mHop), a mean error correction based on calculating the index of refraction at the transmitter (IRM), the Bouska-Raquet model (BR), and lastly a case where no tropospheric delay model is applied. Figure 4.7 plots the tropospheric delay correction that is applied to LPRN1400 for each of the tropospheric models discussed.

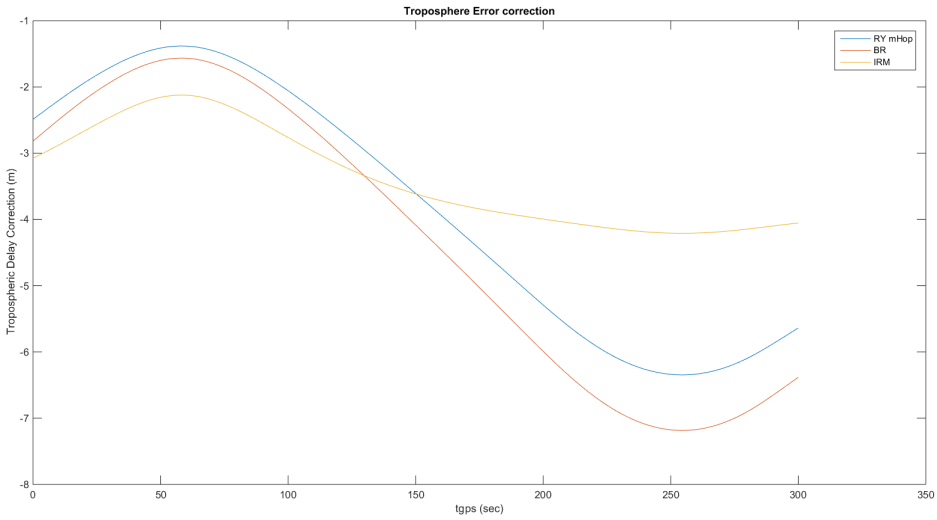

Figure 4.7. Tropospheric Delay correction Applied to LRPN 14 over Sample Period

Figure 4.7 shows that the ray-traced approach of the modified Hopfield model and the Bouska-Raquet model bear similar tropospheric delay model corrections. The calculated index of refraction method for pseudolites produce the same general shape to that of the RT mHop approach and the BR approach; however, has a flatter change in magnitude when calculating varying distances. From analysis in Chapter 3, the ray-tracing modified Hopfield model (RT mHop) and the index of refractivity model (IRM) proved to work the best of the three models when calculated using the raw measurements. The Figure 4.7 shows the troposphere corrections that were used in the sample period that were applied to LPRN 1400.

4.4 Navigation Solution Tests

Flight Test Set-up.

Data collected during the flight test for the UHARS consisted of flying a criss-crossing pattern over the test range, shown in Figure 4.8. The aircraft attempted to make the turns not to exceed a roll angle of 25 degrees to minimize the aircraft

masking as discussed above in Section 4.2. The roll of the aircraft during the flight over the range is shown in Figure 4.9.

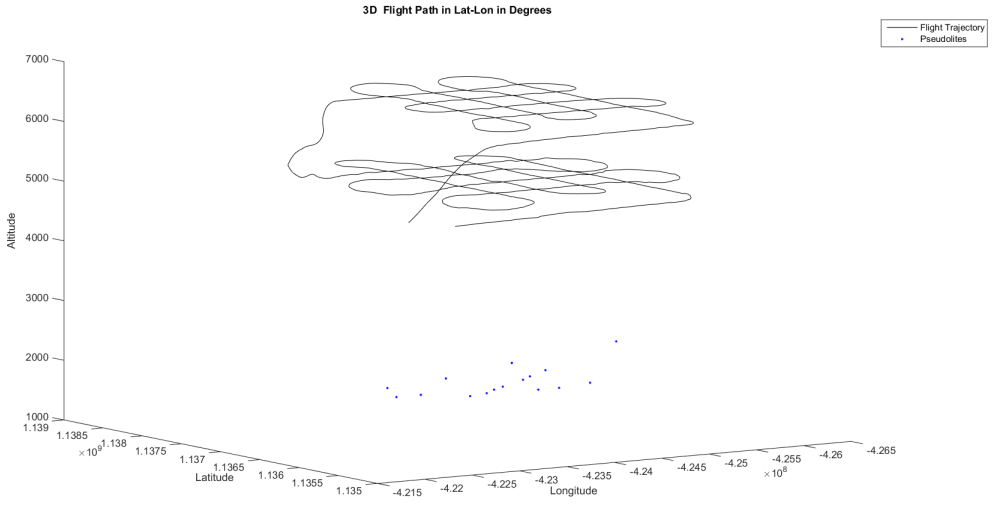

Figure 4.8. 3-D Flight Trajectory Sample Trajectory With Pseudolites

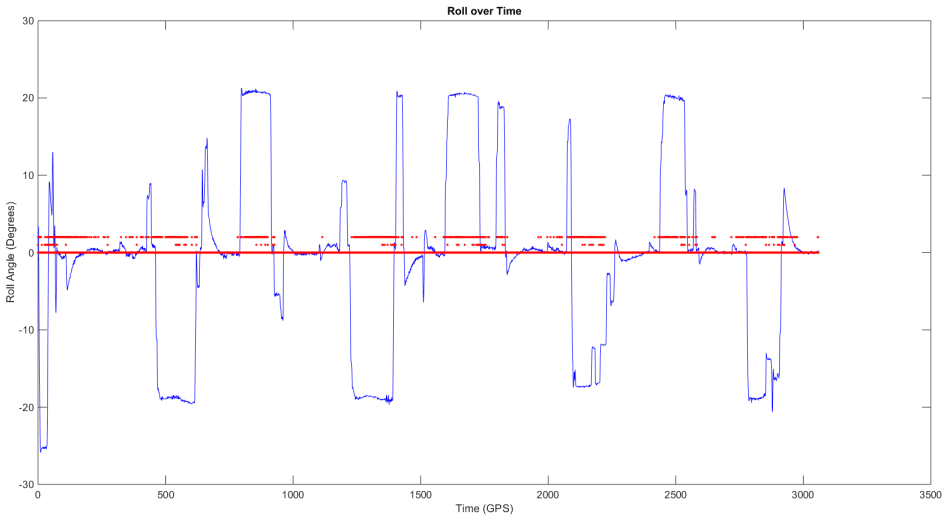

Figure 4.9. Aircraft Roll Angle and Cycle Slip vs Time

As previously discussed, the UHARS EEGI INS is as the inertial. Constant biases are evident in the IMU plot which is inductive of an IMU misalignment [27].

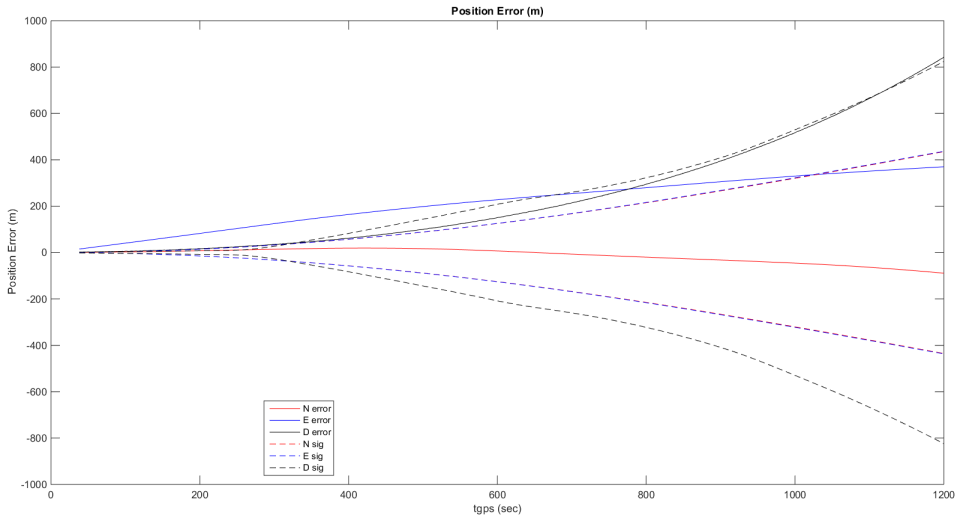

Figure 4.10. Position Error of IMU Propagation

From Figure 4.10, the values for a tactical-grade, IMU preform adequately for a tactical-grade inertial[2].Evidence of the down direction drifting past the accepted values appear to be evident over time. This is likely caused by a misalignment of the IMU or an unmodeled lever arm.

Developed Tests .

In order to provide a comparison of the effectiveness of the developed algorithm's measurement model, cycle slip detection and repair process and tropospheric delay correction, six test were developed. Lever arms are applied from the EEGI on the UHARS rack to the Cooper antenna, which receive dthe Locata pseudolites signals. The filters initial position, velocity, and attitude is initialized from the truth reference for that instant in time. The truth reference that is used to compare the filter solution was the 746Th Test Squadron blended solution that also originates at the EEGI on the UHARS rack. This allows the filter generated solution and truth reference solution to have the same origin and therefore no additional lever arms are required to be

applied. The tropospheric delay models, slip thresholds, and number of pseudorange updates recorded after a cycle slip, as described in Section 3.6 in Chapter III, vary in each test. A breakdown of the tests are in Table 4.1 with varying tropospheric models, cycle slip thresholds, and pseudorange updates after a cycle slip occurs.

Table 4.1. Developed Tests for Comparison

Scenarios			
	Trop. Model	cycles	PR updates
Scenario 1	None	3	2
Scenario 2	RT mHop	1.5	2
Scenario 3	RT mHop	3	2
Scenario 4	RT mHop	3	0
Scenario 5	RT mHop	3	∞
Scenario 6	IRM	3	2

The term RT mHop refers to the ray-tracing method of the modified Hopfield model, and the term IRM, refers to the index of refractivity model developed. Since the tropospheric correction between the RT mHop and the BR model were close, only the RT mHop model was used in the tests developed. The sample period chosen for the flight tests were North-South flights shown in Figure 4.11. The blue circles represent the pseudolite locations, and the red line shows the flight path that begins on the bottom right of the plot and continues toward the left. For each test, the position error and measurement residuals are plotted for comparison.

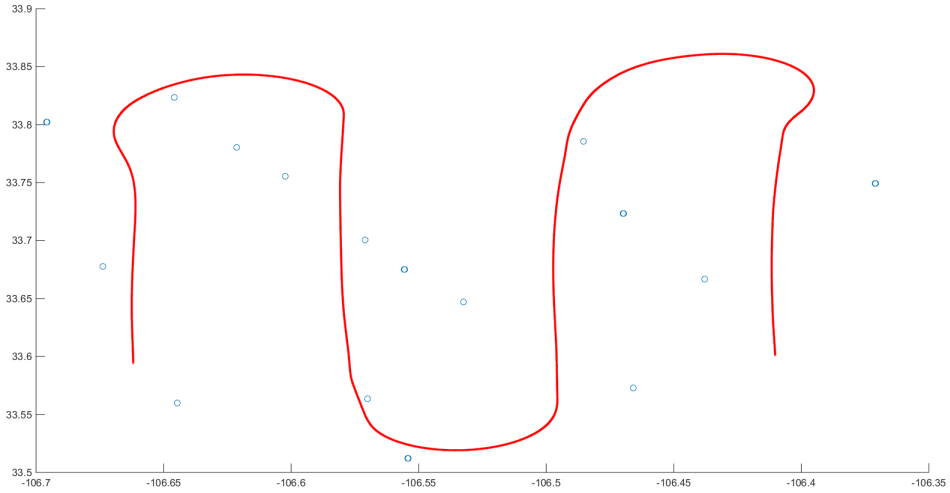

Figure 4.11. 2-D Flight Trajectory During Test Peroid with Pseudolites

Analysis of Developed Tests.

After the six tests are established above, the position results are plotted in this section, analyzed and compared. Further, the filters residuals are plotted and compared. Together, plots proved a measure of the navigation filter effectiveness.

Test 1.

The first scenario, does not apply a tropospheric model, and uses two pseudorange updates after a cycle-slip with a cycle-slip threshold set to 3 cycles. Figure 4.12, plots Test 1's position error.

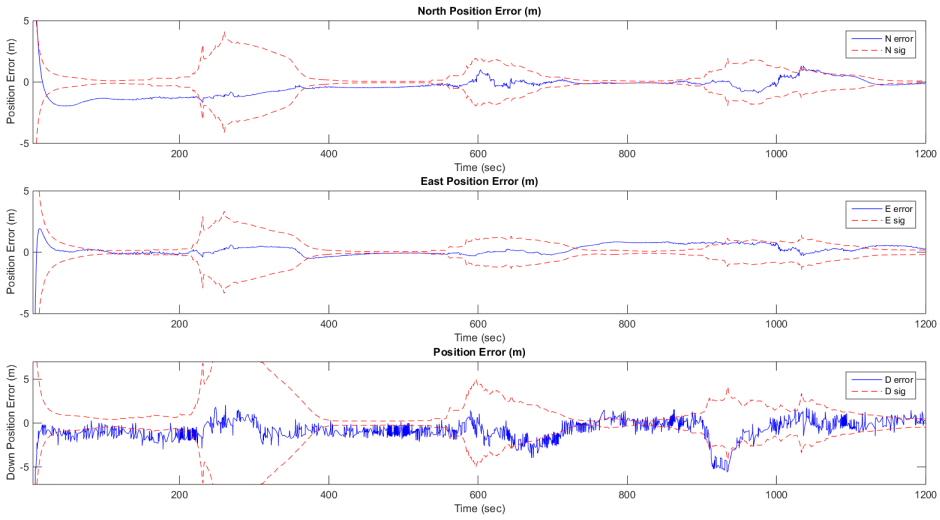

Figure 4.12. Position Error of Test 1. No tropospheric delay model applied, with a slip threshold of 3 cycles and 2 pseudorange updates upon clcyle slip reset.

When examining the position error upon initialization, in all the North, East and down directions the error rapidly decreases as the filter converges to a navigation solution. In the north direction that the error continues to exceed the uncertainty expected; however, the error's magnitude decreases over time, and converges to an error value within the sigma values. The east position error begins to drift as time continues. Lastly, the down direction error appears constant, only slightly improving with time, appearing to have a near constant bias. The error is most likely attributable to tropospheric error model and/or unmodeled lever arms. Some of the tropospheric error in this test are absorbed into other bias error terms. Figure 4.13 shows the carrier phase residuals of test 1.

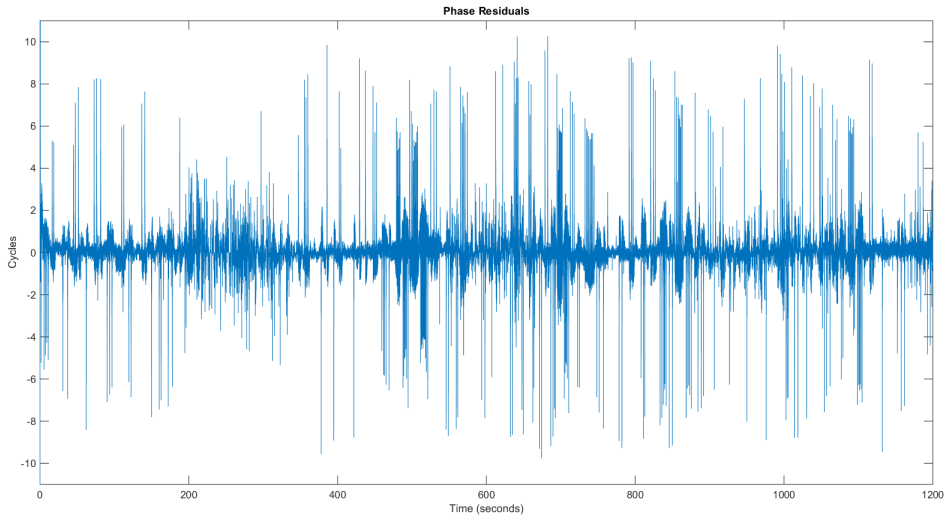

Figure 4.13. Carrier Phase Measurement Residuals of Test 1

Test 2.

The filter residual errors peaked during the cycle clip repair process. Somewhat higher residuals were expected, based on the position error, which indicated that the filter converged onto a solution with inherent error.

In test 2, the modified Hopfield tropospheric delay model was added with again two pseudorange measurements added after a cycle slip, and a cycle slip threshold of 1.5 cycles is set. The position error is shown in 4.14.

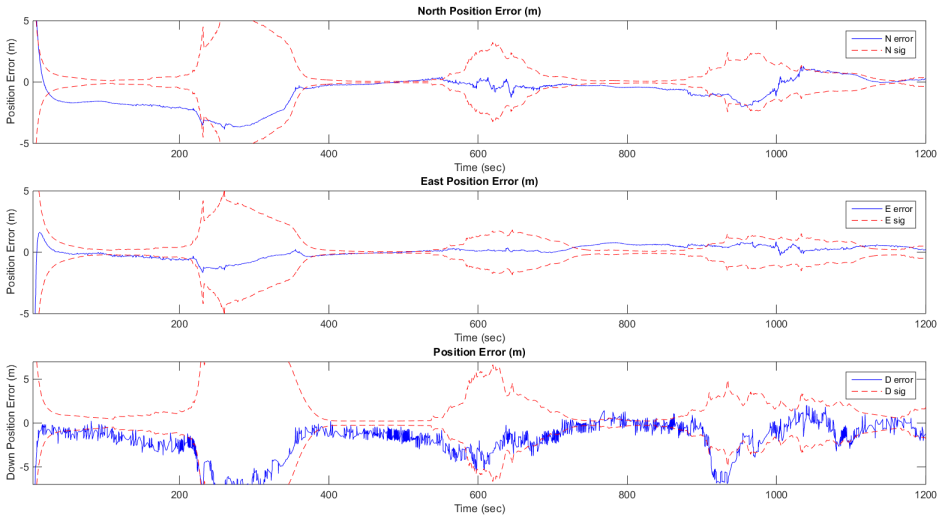

Figure 4.14. Position Error of Test 2. RT mHoptropospheric delay model applied, with a slip threshold of 1.5 cycles and 2 pseudorange updates upon clcyle slip reset.

The position error general magnitudes in all directions are relatively consistent. Some indication of an additional lever arm that is not modeled appears to exist as the error in the east direction is affected by the direction of flight. The carrier phase residuals are plotted in 4.15.

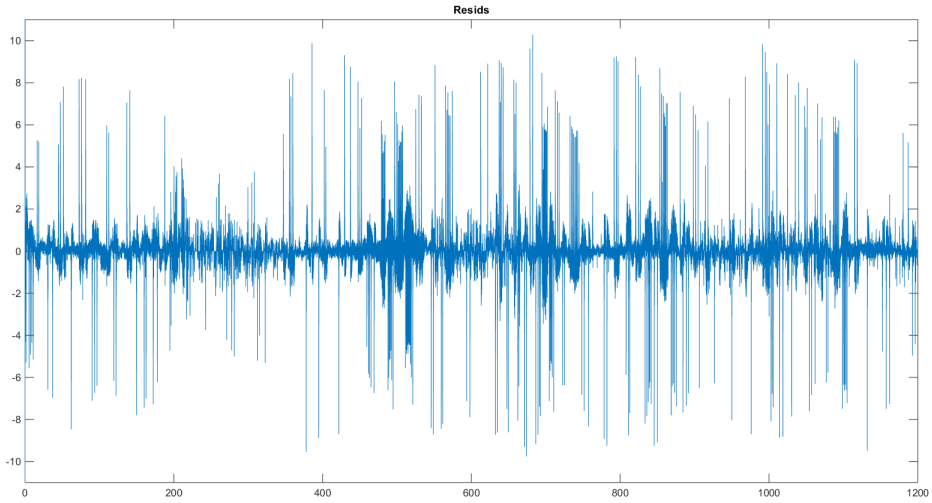

Figure 4.15. Carrier Phase Measurement Residuals of Test 2

The filter residuals look very similar to that of the first scenario, despite a tropospheric delay model being added. Figure 4.15 show that the residuals spike during cycle slips, and quickly return to low (less than 2) values.

Test 3.

Test 3 is much like Test 2, however, a looser slip threshold of 3 cycles is applied. The position error is shown in Figure 4.16.

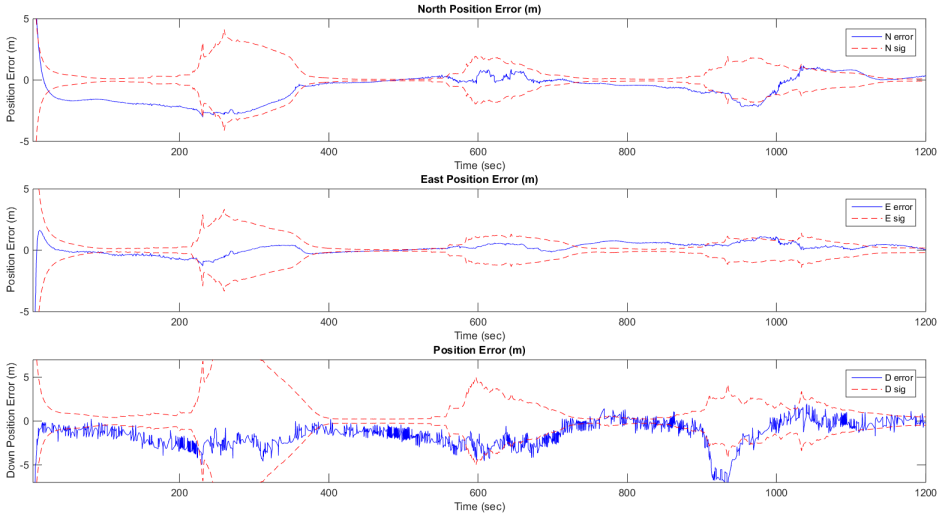

Figure 4.16. Position Error of Test 3. RT mHop tropospheric delay model applied, with a slip threshold of 3 cycles and 2 pseudorange updates upon clcyle slip reset.

The looser slip threshold overall appear to have small effect on the position error. Without further statistical analysis, little in inferred about the position error. Figure 4.17 shows the carrier phase measurement residuals.

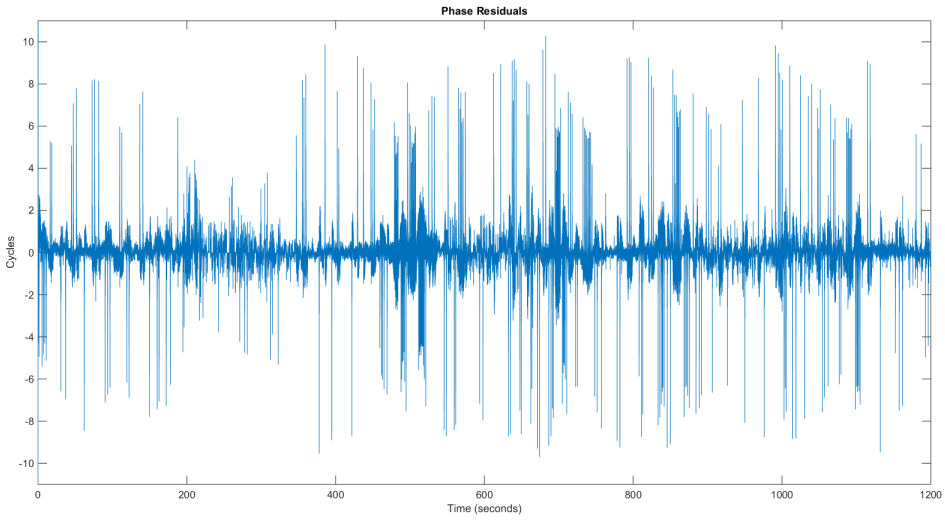

Figure 4.17. Carrier Phase Measurement Residuals of Test 3

Upon comparison of the carrier phase residuals of Figure 4.15 and Figure 4.17 insignificant change is visible seen. This infers that the change of a slip threshold from 1.5 cycles to 3 cycles has a small effect on the overall solution accuracy and performance.

Test 4.

Test 4 also closely follows Test 2, with the exception that this test does not incorporate any pseudorange measurements. The strictly carrier phase position solution is shown in Figure 4.18.

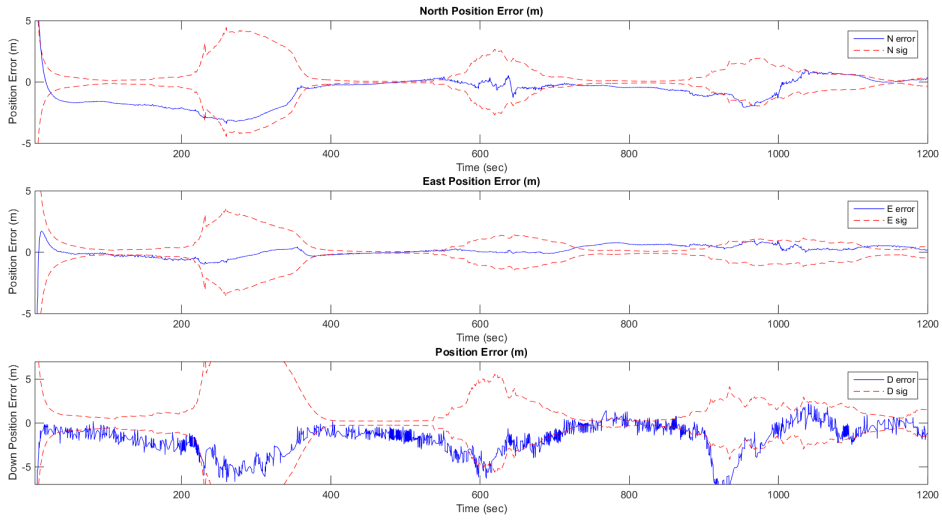

Figure 4.18. Position Error of Test 4. RT mHop tropospheric delay model applied, with a slip threshold of 3 cycles and no pseudorange updates upon clcyle slip reset.

The position solution for this test had smaller sigma values since the carrier-phase sigma value was set to 0.07 meters and a slightly worst position estimate as shown in Figure 4.18 when compared against Figure 4.14. The measurement residuals are shown in Figure 4.19 for this test.

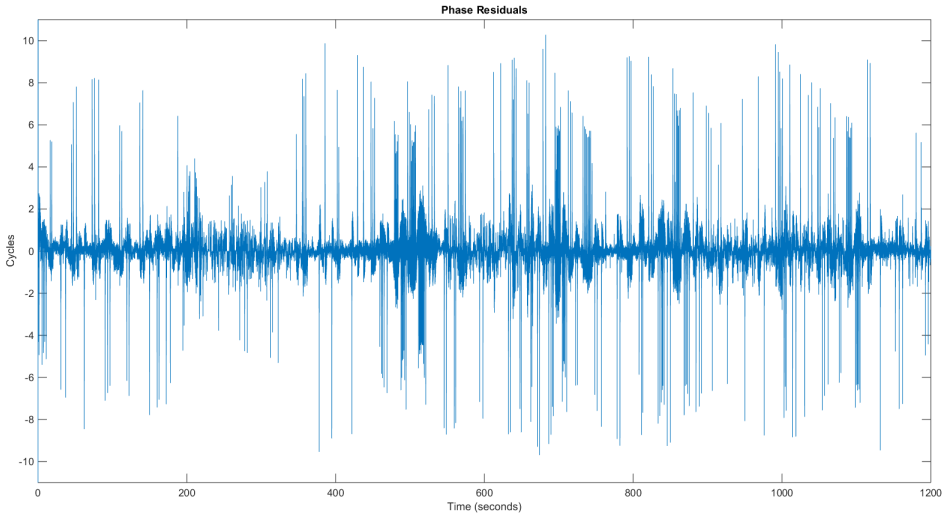

Figure 4.19. Carrier Phase Measurement Residuals of Test 4

Figure 4.19 again to have the larger residual errors during cycle slips then converge to low values (less than 2) as in previous test cases.

Test 5.

Test 5, much like Test 4, closely follows Test 2, however, incorporates every available pseudorange measurement. The postion error of Test 5 is shown in Figure 4.20.

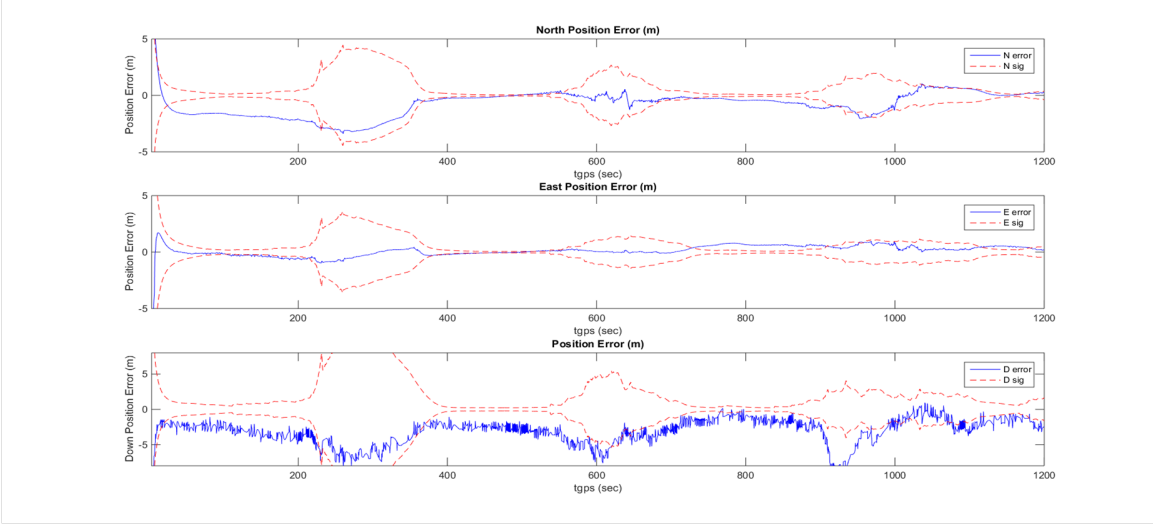

Figure 4.20. Position Error of Test 5. RT mHop tropospheric delay model applied, with a slip threshold of 3 cycles and an infinite number of pseudorange updates upon clcyle slip reset.

Since the pseudorange measurements are noisy, a higher uncertainty (4 meters) is assigned to them. The filters position solution stayed within the higher bounds, although the overall accuracy was not improved. Figure 4.21 shows the pseudorange residuals and Figure 4.22 shows only the carrier-phase residuals.

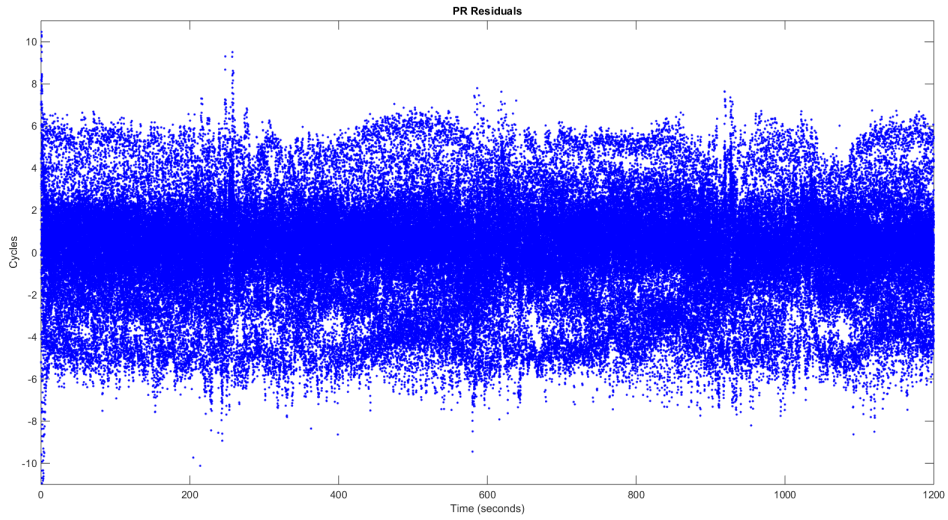

Figure 4.21. Pseudorange Residuals of Test 5. IRM tropospheric delay model applied, with a slip threshold of 3 cycles and unlimited pseudorange updates upon clcyle slip reset.

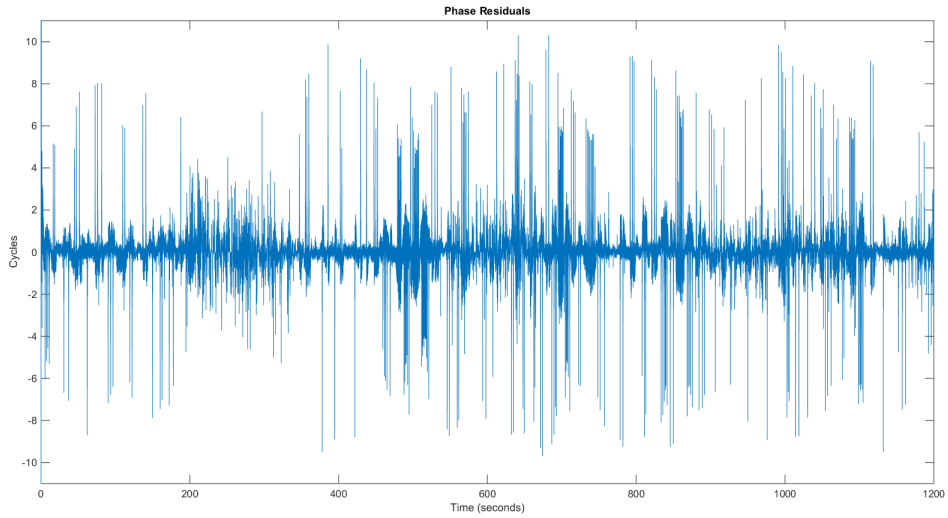

Figure 4.22. Phase Residuals of Test 5. IRM tropospheric delay model applied, with a slip threshold of 3 cycles and unlimited pseudorange updates upon clcyle slip reset.

The carrier-phase residuals shown in Figure 4.22 follow very closely to the previous test residuals. The pseudorange residuals are much higher than the carrier-phase

residuals as shown in 4.21 due to the noisy nature of pseudorange measurements.

Test 6.

Lastly, Test 6 closely followed Test 2 using a cycle threshold of 3 cycles, and incorporating two pseudoranges after a cycle slip; however, this model uses the index of refrativity tropospheric delay model. . Figure 4.23 plots the position error for this test.

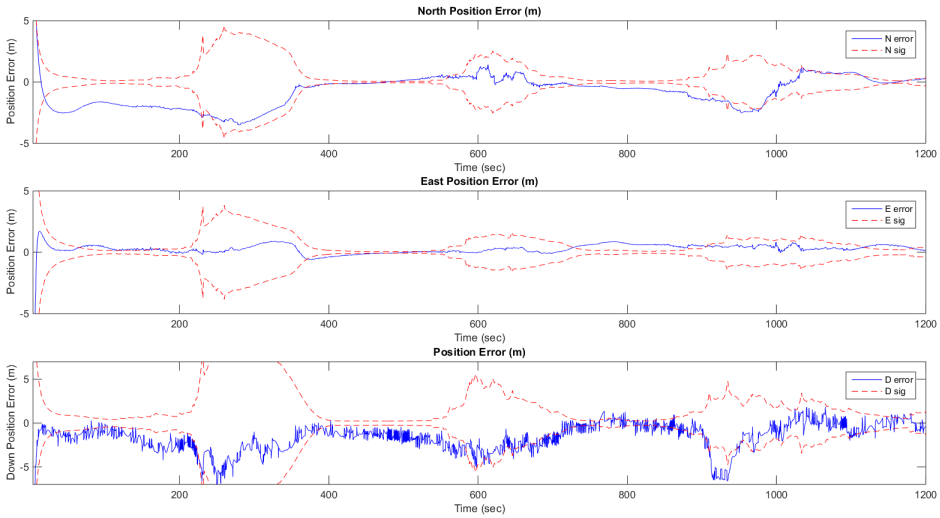

Figure 4.23. Position Error of Test 6. IRM tropospheric delay model applied, with a slip threshold of 3 cycles and two pseudorange updates upon clcyle slip reset.

Test's 6 appeared to have the much worst overall results in terms of position error visibly seen in Figure 4.23. This indicates that the tropospheric delay model preformed less well than that of the ray-tracing modified Hopfield model. The carrier-phase measurement residuals shown in Figure 4.24.

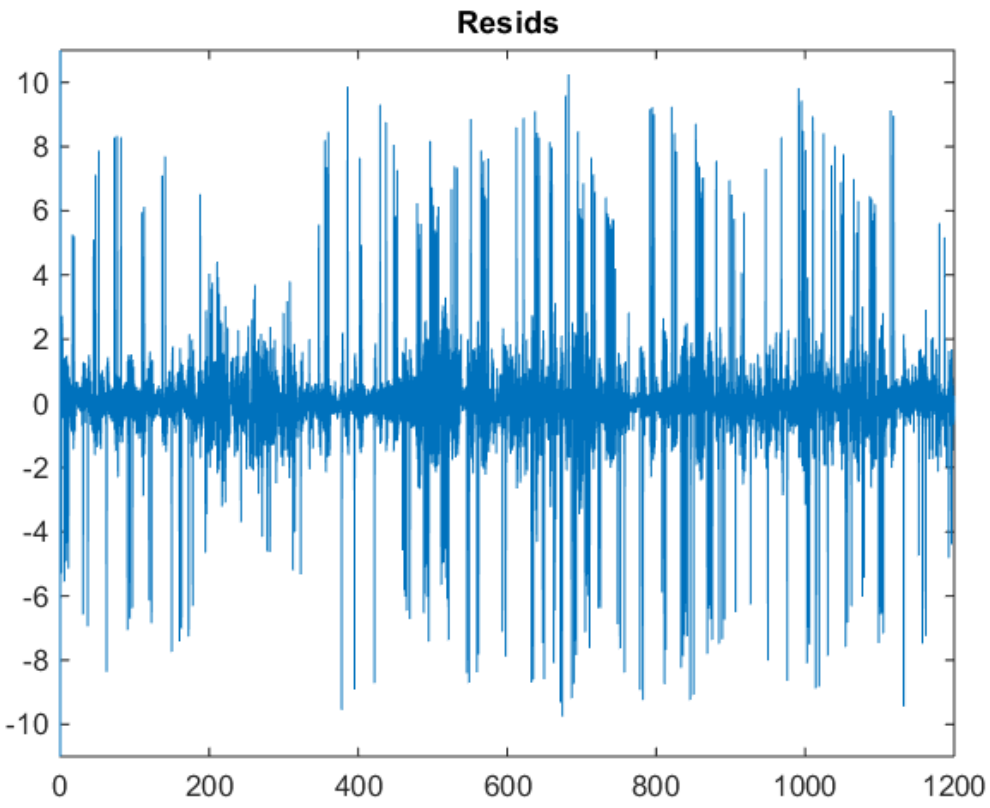

Figure 4.24. Carrier Phase Measurement Residuals of Test 6

Although the position error was significantly higher as the previous tests, the carrier phase measurement residuals appeared only slightly worst (higher).

Summary of Tests.

From analysis, a level arm appears to be unaccounted for between the navigation solution and the truth. This is evident from the correlation between the direction of error in the position error plot and the heading of the aircraft. Error that exist from a lever arm does not account for all the error that exists. As the aircraft travels along the outer edge of the Loclite array, the error grows in magnitude. This trend is visible from all six tests performed.

2DRMS and 3DRMS Analysis.

The 2D and 3DRMS are good metrics for postion accuracy[15]. The 2DRMS uses the north and east position errors only are are calculated by using 4.1. the 3DRMS incorporates a 3-axis postion accuracy metric and is calculate using Equation 4.2. The δP_n, the δP_n, and the δP_n terms represent the position errors in north, east and down direction respectively.

$$2D - RMS = \sqrt{\delta P_n^2 + \delta P_e^2} \tag{4.1}$$

$$3D - RMS = \sqrt{\delta P_n^2 + \delta P_e^2 + \delta P_d^2} \tag{4.2}$$

The mean of the tests were were also compared againt a single pass in the center of the Loclite array. This single pass took place over a 200 second period and is plotted below in Figure 4.25.

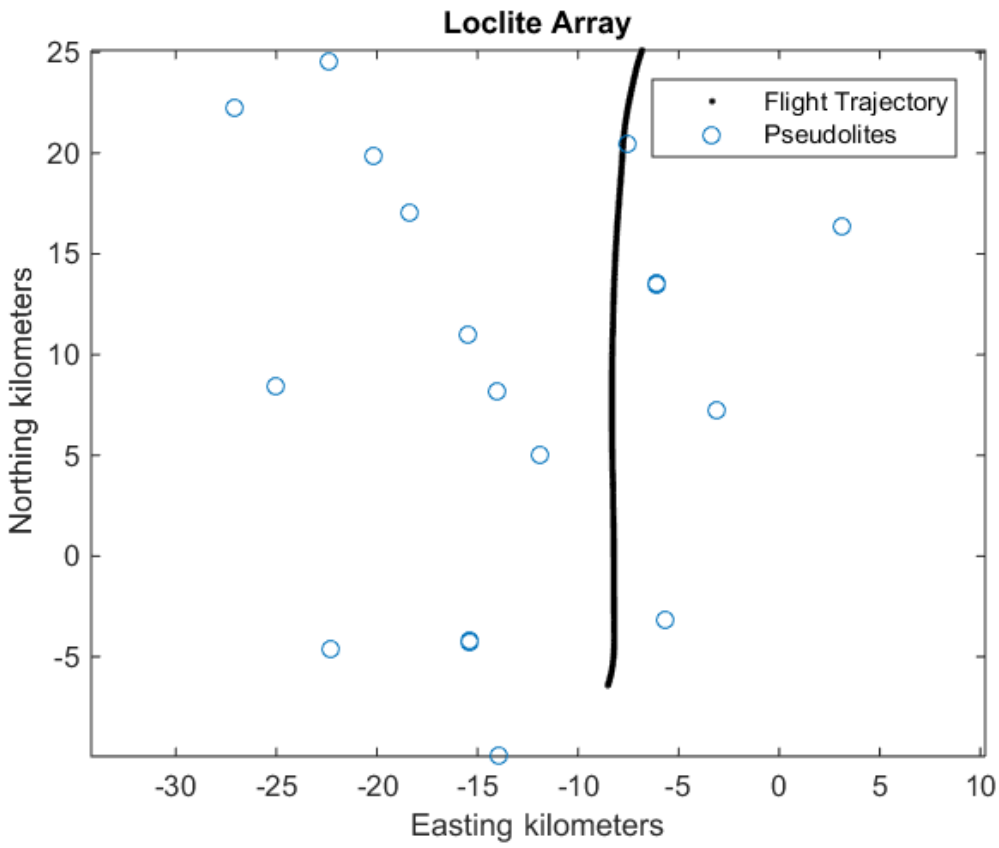

Figure 4.25. Center Pass Flight Trajectory

The 2D and 3DRMS were compared to one another taking the mean of each test and during the center pass over a 200 second period.

Table 4.2. 2D and 3D Root Mean Square Errors

	2DRMS		3DRMS	
Test	Center Pass (m)	Period Mean (m)	Center Pass (m)	Period Mean (m)
1	0.50	0.74	0.74	1.63
2	0.26	0.74	0.59	2.05
3	0.21	0.59	0.57	1.51
4	0.23	0.2852	0.62	0.55
5	0.24	.0.61	0.60	1.61
6	0.31	0.71	0.71	1.97
7	0.18	0.60	0.45	1.36

Dilution of Precision - DOP.

The dilution of precision (DOP) is analyzed to estimate how much the measurement error will affect the final state estimation. The DOP is simply a magnifying effect based on the geometry of the transmitters. More accurately, the DOP is based on the covariance matrices and the clock error. To find the DOP the user to pseudolite the equation is first linearized to a nominal user position as defined in Equation 4.3.

$$\begin{aligned} r_u^p = \quad & r_{u0}^p - \tfrac{x^s - x_{u0}}{r_{u0}^s}\Delta x_u - \tfrac{y^p - y_{u0}}{r_{u0}^p}\Delta y_u \\ & - \tfrac{z^p - z_{u0}}{\rho_{u0}^p}\Delta z_u + c\Delta t_u \end{aligned} \tag{4.3}$$

In the above equation, the p term represents the pseudolite, where the u term refers to the user in the local level frame, the 0 subscript represents the nominal position, r is the range respect to the nominal user position, x, y, z are axis positions and $c\Delta t_u$ is the clock error in units of meters. The linearized ranging equation is shown in equation 4.3 and is rearranged to have the form $\Delta\rho = \mathbf{H}\Delta\mathbf{x}_u$. The DOP is

preformed by calculating the variances by preforming $\mathbf{D} = (\mathbf{H}^T\mathbf{H})^{-1}$. The diagonals represents the covariance of one axis $D_{11} = \sigma_x^2$, $D_{22} = \sigma_y^2$, and $D_{33} = \sigma_z^2$.

The variances required for calculating the DOP is obtained from the this matrix $\mathbf{D} = (\mathbf{H}^T\mathbf{H})^{-1}$. Each diagonal represents the covariance of one axis $D_{11} = \sigma_x^2$, $D_{22} = \sigma_y^2$, etc. The equation for the different types of DOP that were implemented in this research are shown in 4.4.

$$DOP = \begin{array}{c} Position\ DOP \\ = \sqrt{D_{11} + D_{22} + D_{33}} \\ Horizontal\ DOP \\ = \sqrt{D_{11} + D_{22}} \end{array} \tag{4.4}$$

The DOP values were calculate at the center of the range, the northern fringe of the range, and over one of the tests. Figure 4.26 depicts where the DOP measurements at the Northern fringe and center postions.

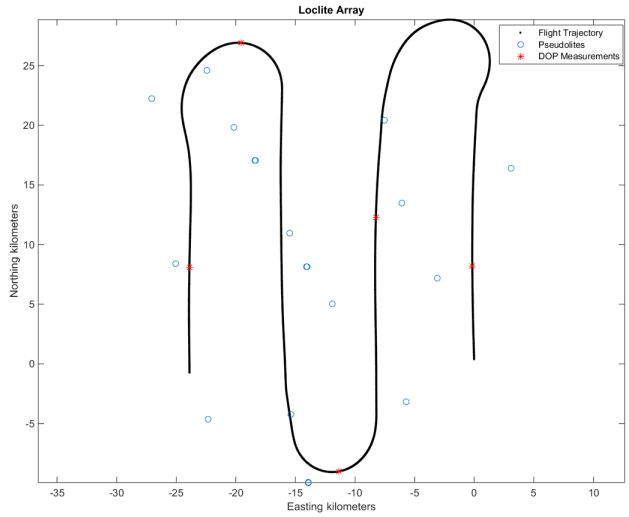

Figure 4.26. Flight trajectory showing positions where DOP was measured

Table 4.3 show the sample DOP values taken at the center, norther edge of the

array, and the period mean. Figure 4.26 shows the DOP values over the test period.

Table 4.3. Sample Dilution of Precision Values

Calculated Dilution of Precision						
	Center	N	E	S	W	Mean
HDOP	0.62	1.89	1.67	1.721	1.62	1.43
PDOP	1.42	3.13	2.97	2.95	2.98	2.58

4.5 Summary

This chapter discussed the navigation filter parameters, description of the test developed and result. This research is the first time that Locata pseudolites were tightly-coupled with an IMU in an aircraft scenario. No single test proved to obtain the desired results of decimeter level position accuracy which was indicative of unmodeled errors. This leads to the conclusion that unmodeled errors exist preventing the desired decimeter level of accuracy to be achieved.

V. Conclusions and Recommendations

5.1 Conclusions

This thesis presented the initial implementation of a tightly-coupled Locata pseudolite/INS for developing a navigation solution for the UHARS program. The objective of decimeter-level accuracy navigation solution results was not obtained for any the test cases performed. Sub-meter accuracy, however, was consistently achieved which indicates unmodeled errors still exist within the solution. The tropospheric delay model, unmodeled lever arms, and filter tuning are likely causes of the solution not to receive the desired level of accuracy expected for a carrier-phase measurements solution.

A cycle slip detection and repair process was implemented for detecting failures in pseudolite phase measurements. The pseudolite suffered from a high rate of cycle slips and the implemented cycle slip detection and repair process appeared to work well. The ambiguities states under the tests parameters provide tracked well give the parameters. Using a cycle slip threshold between 1.5 to 3 cycles both proved to lead to submeter-level accuracy. In Chapter IV when the slip threshold was extended to 5 cycles, the position error increased as error was introduced into the filter by the looser threshold value.

A further exploration of a tropospheric models can decrease the position error as well. The index of refraction method faired worse than that of the ray-traced modified Hopfield model and the Bouska-Raquest model whose results closely followed that of the the ray-traced modified Hopfield model.

Since there appeared to be constant biases in the position error depending on the flight heading, unmodeled lever arms were the likely cause. Further, this appeared as a reoccuring source of error for every test case developed, thus making the possibility

unlikely that other error factors were leading to the constant biases.

Lastly, the carrier-phase solution with only a few pseudorange updates preformed better than that of the test case where every pseudorange available was used.

5.2 Recommendations for Future Research

There exist several recommendations for future research. Each recommendation will further the advance the research and quality of the navigation solution

- The ray-tracing modified Hopfield tropospheric delay model, as described in Chapter III, may have preformed better if data was available for temperature, pressure, and relative humidity changes were recorded over the path of the signal transmission, rather than only available at the transmitters location. Given the change in temperature, pressure, and relativity, a more accurate tropospheric delay model can be achieved.

- Implementing software for the Kalman filter to accept dual frequencies. The implemented filter in this research only used one of the two transmitted frequencies. By using both frequencies, a more robust cycle slip algorithm can be developed. Further, using dual frequencies can lead to several other opportunities to increase filter accuracy.

- Filtertuning should be continued in order to improve filter performance.

- Lever arms should be either re-measured, or, alternatively, lever arms could be estimated in the filter in order to reduce errors due to lever arms error.

Bibliography

1. Ahmed, Mohammed Mushthaq, Quddusa Sultana, A Supraja Reddy, and MA Malik. "Tropospheric error correction in assisted GPS signals". *Indian Journal of Radio & Space Physics*, 42:159–166, 2013.

2. Alkhaldi, Capt Humood. *Integration of a Star Tracker and Inertial Sensors Using an Attitude Update*. Master's thesis, Air Force Institute of Technology.

3. Amt, John H. *Methods for aiding height determination in pseudolite-based reference systems using batch least-squares estimation*. Master's thesis, Air Force Institute of Technology.

4. Amt, John HR and John F Raquet. "Flight Testing of a Pseudolite Navigation System on a UAV". *ION Conference, Jan.* 2007.

5. Barnes, J, C Rizos, J Wang, D Small, G Voigt, and N Gambale. "LocataNet: Intelligent time-synchronised pseudolite transceivers for cm-level stand-alone positioning". *Satellite Navigation and Positioning (SNAP) Group, School of Surveying and Spatial Information Systems, The University of New South Wales, Australia (UNSW)*, 2003.

6. Barnes, Joel, Chris Rizos, Jinling Wang, David Small, Gavin Voigt, and Nunzio Gambale. "Locata: the positioning technology of the future". *Proceedings of the 6th Iinternational Symposium on Satellite Navigation Technology Including Mobile Positioning & Location Services, Melbourne, Australia July*, 2003.

7. Bouska, Terry J. *Development and Simulation of a Pseudolite-based flight Reference System*. Master's thesis, Air Force Institute of Technology.

8. Bouska, Terry J and John F Raquet. "Tropospheric Model Error Reduction in Pseudolite-Based Positioning Systems". *Proceedings of the 16th International Technical Meeting of the Satellite Division of The Institute of Navigation (ION GPS/GNSS 2003)*, 390–398. 2001.

9. Brown, R.G. and P.Y.C. Hwang. *Discrete Kalman Filter Basics, 4th Edition*. IEE radar, sonar, navigation, and avionics series. J. Wiley and Sons, 2012.

10. Ciampa, Michael A. *Failure Detection of a Pseudolite-Based Reference System Using Residual Monitoring*. Master's thesis, Air Force Institute of Technology.

11. Craig, Desiree, Derek Ruff, Steve Hewitson, Joel Barnes, and John Amt. "The UHARS Non-GPS Based Positioning System". *Inside GNSS*, 2011.

12. Crawford, Matthew P. *Optimal Geometric Deployment of a Ground Based Pseudolite Navigation System to Track a Landing Aircraft*. Master's thesis, Air Force Institute of Technology.

13. Dai, Liwen, Jinling Wang, Toshiaki Tsujii, and Chris Rizos. "Pseudolite applications in positioning and navigation: Modelling and geometric analysis". *Int. Symp. on Kinematic Systems in Geodesy, Geomatics & Navigation (KIS2001)*, 482–489. 2001.

14. England, Gordon. "National Coordination Office For Space-Based Positioning, Navigation And Timing". url-http://http://www.gps.gov/governance/excom/charter/annex/, December 2006. [Online; accessed 15-January-2015].

15. Groves, P.D. *Principles of GNSS, Inertial, and Multisensor Integrated Navigation Systems*. GNSS technology and applications series. Artech House, 2008.

16. Hyoungmin So, Kiwon Song, Junpyo Park. "Performance Analysis of Pseudolite Tropospheric Delay Models Using Radiosonde Meteorological Data". *Journal of the Korean GNSS Society*, 2:49–57, 2013.

17. Kaplan, E. and C. Hegarty. *Understanding GPS: Principles and Applications, Second Edition*. Artech House, 2005.

18. Littleton, 1st Lt Shawn D. and Capt Jeremiah A Shockley. "Emerging T&E Capabilities Shortfall for GPS-Denied Tests and Possible Solutions".

19. Maybeck, Peter S. *Stochastic Models, Estimation, and Control, Vol I.* Mathematics in Science and Engineering. Academic Press, Inc., 1979.

20. Maybeck, Peter S. *Stochastic Models, Estimation, and Control Volume 2*, volume 3. Academic press, 1982.

21. Neu, Jonathon. *A tightly-coupled INS/GPS integration using a MEMS IMU*. Master's thesis, Air Force Institute of Technology.

22. Noureldin, Aboelmagd, Tashfeen B Karamat, and Jacques Georgy. *Fundamentals of inertial navigation, satellite-based positioning and their integration*. Springer Science & Business Media, 2012.

23. Shockley, Capt Jeremiah A and Lt Scott Zetterstrom. "50 Years of the Central Inertial and GPS Test Facility". *US Air Force T&E Days 2009*.

24. Shockley, Jeremiah A. *Estimation and Mitigation of Unmodeled Errors for a Pseudolite Based Reference System*. Master's thesis, Air Force Institute of Technology.

25. Smearcheck, M., D. Marietta, J. Raquet, D. Ruff, and A Herrera. "Expandable Flight Reference Data Processing Software *Joint Navigation Conference 2014*", 2014.

26. Snodgrass, Britt and John Raquet. "The CIGTF High Accuracy Post-Processing Reference System (CHAPS)". *Proceedings of the 7th International Technical Meeting of the Satellite Division of The Institute of Navigation (ION GPS 1994)*, 755–763. 1994.

27. Titterton, D., J.L. Weston, and Institution of Electrical Engineers. *Strapdown Inertial Navigation Technology, 2nd Edition*. IEE radar, sonar, navigation, and avionics series. Institution of Engineering and Technology, 2004.

28. Trunzo, Angelo, Robert Ramirez, and pages=3582-3586 year=2011 Baldwin, Jason journal=Proceedings of the 24th International Technical Meeting of The Satellite Division of the Institute of Navigation (ION GNSS 2011). "The UHARS Non-GPS Based Positioning System (NGBPS)".

29. Van Dierendonck, AJ. "GPS receivers". *Global Positioning System: Theory and Applications.*, 1:329–407, 1996.

30. Veth, Michael J. *Fusion of imaging and inertial sensors for navigation*. Ph.D. thesis, Air Force Institute of Technology.

31. Wang, Jianguo Jack, Jinling Wang, David Sinclair, Hung Kyu Lee, et al. "Tropospheric Delay Estimation for Pseudolite Positioning". *Positioning*, 1(09), 2005.

32. Wang, Jinling, Toshiaki Tsujii, Chris Rizos, Liwen Dai, and Michael Moore. "GPS and pseudo-satellites integration for precise positioning". *Geomatics Research Australasia*, 74:103–117, 2001.

REPORT DOCUMENTATION PAGE

Form Approved
OMB No. 0704–0188

1. REPORT DATE *(DD–MM–YYYY)*	2. REPORT TYPE	3. DATES COVERED *(From — To)*
26–03–2015	Master's Thesis	Oct 2013 — Mar 2015

4. TITLE AND SUBTITLE

Initial Implementation And Testing Of A Tightly-Coupled IMU/Pseudolite System

5a. CONTRACT NUMBER

5b. GRANT NUMBER

5c. PROGRAM ELEMENT NUMBER

6. AUTHOR(S)

Kawecki, James E.C., Capt, USAF

5d. PROJECT NUMBER

15G-288

5e. TASK NUMBER

5f. WORK UNIT NUMBER

7. PERFORMING ORGANIZATION NAME(S) AND ADDRESS(ES)

Air Force Institute of Technology
Graduate School of Engineering and Management (AFIT/EN)
2950 Hobson Way
WPAFB OH 45433-7765

8. PERFORMING ORGANIZATION REPORT NUMBER

AFIT-ENG-MS-15-M-025

9. SPONSORING / MONITORING AGENCY NAME(S) AND ADDRESS(ES)

746th Test Squadron
1644 Vandergrift Road
Blgd 1625
Holloman AFB, NM 88330-7850
Phone (575) 679-1668
Email: Angelo.Trunzo@us.af.mil

10. SPONSOR/MONITOR'S ACRONYM(S)

746 TS/TGGA

11. SPONSOR/MONITOR'S REPORT NUMBER(S)

12. DISTRIBUTION / AVAILABILITY STATEMENT

DISTRIBUTION STATEMENT A:
APPROVED FOR PUBLIC RELEASE; DISTRIBUTION UNLIMITED.

13. SUPPLEMENTARY NOTES

14. ABSTRACT

Currently, the 746th Test Squadrons (746th TS) Central Inertial and GPS Test Facility (CIGTF) operates one of the most accurate truth reference systems, called the CIGTF Reference System (CRS). CIGTF will be replacing the CRS with a new references system called UHARS (Ultra High Accuracy Reference System). UHARS will differ from CRS by adding the ability to use a non-GPS pseudolite system, as a new measurement source. This research effort describes the design of the extended Kalman filter which is developed in AFIT's SPIDER filter framework which implements a tightly-coupled pseudolite/INS filter.

15. SUBJECT TERMS

non-GPS, navigation, reference system, thesis, pseudolites

16. SECURITY CLASSIFICATION OF:			17. LIMITATION OF ABSTRACT	18. NUMBER OF PAGES	19a. NAME OF RESPONSIBLE PERSON
a. REPORT	b. ABSTRACT	c. THIS PAGE			Dr. J. F. Raquet, AFIT/ENG
U	U	U	U	84	19b. TELEPHONE NUMBER *(include area code)* (937) 255-3636, x4683; john.raquet@afit.edu